49th AIAA Aerospace Sciences Meeting including the New Horizons Forum and Aerospace Exposition
4 - 7 January 2011, Orlando, Florida

AIAA 2011-939

Summary of the First AIAA CFD High Lift Prediction Workshop (invited)

C. L. Rumsey*
NASA Langley Research Center, Hampton VA
M. Long†
University of Wyoming, Laramie, WY
R. A. Stuever‡
Hawker Beechcraft Corp, Wichita, KS
T. R. Wayman§
Gulfstream Aerospace Corp, Savannah, GA

The 1st AIAA CFD High Lift Prediction Workshop was held in Chicago in June 2010. The goals of the workshop included an assessment of the numerical prediction capability of current-generation CFD technology/codes for swept, medium/high-aspect ratio wings in landing/take-off (high lift) configurations. 21 participants from 8 countries and 18 organizations, submitted a total of 39 datasets of CFD results. A variety of grid systems (both structured and unstructured) were used. Trends due to flap angle were analyzed, and effects of grid family, grid density, solver, and turbulence model were addressed. Some participants also assessed the effects of support brackets used to attach the flap and slat to the main wing. This invited paper describes the combined results from all workshop participants. Comparisons with experimental data are made. A statistical summary of the CFD results is also included.

I. Introduction

The prediction of high lift flows is a challenge of practical interest to many engineers in the aircraft industry. For configurations that include multiple elements (leading edge slats and trailing edge flaps), the flow physics can be particularly challenging for today's CFD codes and turbulence models. These challenges include wakes in pressure gradients, wake/boundary layer merging, streamline curvature, separated flow, possible unsteady flow, wing-tip vortical flow, and laminar/turbulent transition regions on each element. A survey of the state-of-the-art in prediction of high lift at the beginning of the 2000's can be found in Rumsey and Ying.[1]

Because of the difficulties inherent in accurately predicting high lift flows, it was decided that open international workshops with a common focus would bring experts together and help to advance the state-of-the-art. The long-term objectives of these workshops are: (1) assess the numerical prediction capability (mesh, numerics, turbulence modeling, high-performance computing requirements, etc.) of current-generation CFD technology/codes for swept, medium/high-aspect ratio wings in landing/take-off (high lift) configurations, (2) develop practical modeling guidelines for CFD prediction of high lift flowfields, (3) advance the understanding of high lift flow physics to enable development of more accurate prediction methods and tools, (4) enhance CFD prediction capability for practical high lift aerodynamic design and optimization, (5) provide an impartial forum for evaluating the effectiveness of existing computer codes and modeling techniques, and (6) identify areas needing additional research and development.

The first AIAA CFD High Lift Prediction Workshop (HiLiftPW-1) was held over two days in June 2010 in Chicago, Illinois. The focus of the workshop was on the three-element swept wing tested at NASA, referred to as the NASA Trapezoidal (Trap) Wing model (see Fig. 1). Although parts of the experimental data from two different wind tunnels

*Senior Research Scientist, Computational AeroSciences Branch. Associate Fellow AIAA.
†Applications Engineer. Member AIAA.
‡Senior Principal Multi-Disciplined Engineer, Government Business. Associate Fellow AIAA.
§Technical Specialist - Aerodynamics. Associate Fellow AIAA.

have been used in previous studies,[2–6] collectively the data have never been officially published. This series of workshops was used as an opportunity to further evaluate and analyze some of the existing Trap Wing experimental data. The HiLiftPW-1 committee decided to focus on the data taken in the NASA Langley 14 by 22 foot wind tunnel.

The HiLiftPW-1 was patterned after the successful Drag Prediction Workshop (DPW) series (see, for example, Vassberg et al.[7]). Because grids were often considered to be problematic for the DPW workshops, considerable effort was expended to develop many high-quality grids of different types for HiLiftPW-1. There were seven different grid series supplied up-front for optional use by participants. In addition, the two structured one-to-one grids were translated to unstructured hexahedral format, and one of the tetrahedral unstructured grids was merged into prisms in the boundary layer, forming a mixed-element unstructured grid. Out of these ten different named grid series, nine of them were used by participants. Participants were also allowed to create their own grids.

Details concerning the required computations can be found in Slotnick et al.[8] or on the HiLiftPW-1 website.[a] However, for completeness the required cases are briefly summarized here. A grid study was to be conducted on coarse (C), medium (M), and fine (F) grids for configuration 1 (slat deflected 30°, flap deflected 25°) at angles of attack of $\alpha = 13^\circ$ and 28°. Furthermore, an α sweep from 6° through 37° was to be run using medium-level grids for both configuration 1 and configuration 8 (slat deflected 30°, flap deflected 20°). The Mach number was $M = 0.2$ and Reynolds number based on mean aerodynamic chord was $Re = 4.3$ million. All runs were requested to be "fully turbulent" (no transition modeling), and no tunnel walls were to be included. An optional set of runs included support brackets (supports that connect the slat and flap to the main element).

This paper summarizes the workshop data, including several corrections, modifications, and additions submitted by some of the participants immediately after the workshop. In addition to describing the overall collective results in comparison to experimental data, an attempt is made to identify trends as well as outliers. The paper is organized as follows. First, a summary of the entries is given. Then, an overall view is given of lift curves and polars compared to experiment. Grid convergence behavior is analyzed, followed by a general look at the ability of CFD to predict ΔC_L between configurations. Next, specific surface pressures and skin friction stations are examined, and the effects of support brackets are explored. A statistical analysis is conducted in which scatter limits are calculated. As part of this statistical analysis, the ability to predict the differences between configurations is looked at in greater detail. Finally, conclusions are drawn.

II. Summary of Entries

A summary of the entries to the HiLiftPW-1 are listed in Table 1. It includes an identifier for each submission, the code used, the type of discretization, the grid system, the turbulence model, and other relevant information. All submissions were assigned an entry number, which consists of a primary number in front of the decimal point that identifies the group or person submitting the data, and a secondary sequence after the decimal point that identifies variations (for example, different grids, codes, or turbulence models). There were 21 individuals/groups who submitted 39 entries. However, as noted in the table, some of the entries were incomplete (for example, did not run configuration 8, did not run on three grid levels, etc.). Here, the data set is considered to be "complete" if at least three grid sizes were used for configuration 1 at both $\alpha = 13^\circ$ and 28°, and if at least five angles of attack were run for both configuration 1 and 8 polars. The reasons why participants submitted incomplete data sets were varied: for some it was because they were unable to complete all runs requested, for others it was because they were exploring specific sensitivities or issues and it was not deemed necessary to perform all the computations requested. Both complete and incomplete data sets are included in this summary. For the statistical analysis, all data are included to at least some degree except 003.02, 003.03, 014.03, and 014.05 (each of which were particularly limited CFD studies, denoted by a pound symbol in the table).

In Table 1, the flow solver name and type are listed under "Type." N indicates node-centered Navier-Stokes, C indicates cell-centered Navier-Stokes, and B indicates Lattice-Boltzmann. The grids are identified by two upper-case letters and a number. Some details about the grids will be given below. There were seven participants who included grids with support brackets as part of their computations. In Table 1, the turbulence models referred to under "Turb" are as follows: SA indicates Spalart-Allmaras one-equation, SST indicates Menter Shear Stress Transport k-ω, KE indicates k-ε, KO indicates Wilcox k-ω, RSM indicates Reynolds Stress transport Model, and VLES indicates Very Large Eddy Simulation. A star by the turbulence model means that a variant or special version of the model was employed. These known modifications were as follows: entry 001 included a γ-θ transition model to SST; entry 002 included preconditioning and realizability to k-ε; entries 003.01, 003.02, 003.03, 014.01, 014.02, and 014.03 used an f_{v3} modification with SA; entries 012.01 and 012.02 used no f_{t2} term and included a modification to the production

[a] http://hiliftpw.larc.nasa.gov, accessed 11/22/2010

Table 1. Summary of entries

Entry Number	Code Name	Type	Grid System	Turb Model	Complete?	Brackets?	Notes
001	CFX	N	UX9	SST*	No	No	transition model used, limited config 8
002	CFD++	C	UH13	KE*	Yes	No	
003.01	OVERFLOW	N	SX3	SA*	Yes	Yes	
003.02	OVERFLOW	N	SX3	SA*	No#	No	brackets removed from bracket-like grid
003.03	OVERFLOW	N	SX3	SA*	No#	No	grid study on config 8 at $\alpha = 13^\circ$
004	HIFUN	C	UH14	SA	Yes	No	
005.01	FUN3D	N	UH6	SA	Yes	No	
005.02	NSU3D	N	UH6	SA	No	No	TLNS, no fine grid
006	FUN3D	N	UT5	SA	No	No	no polars
007	TAU	N	UH8	SA	Yes	Yes	
008.01	TAU	N	UH7	SA	No	No	no config 8, no fine grid
008.02	TAU	N	UH7	SST	No	No	no config 8, no fine grid
008.03	TAU	N	UH7	RSM	No	No	no config 8, no fine grid
009	PowerFLOW	B	CB16	VLES	Yes	Yes	transition model used, polars on fine grid
010	EDGE	N	UH8	SA	Yes	Yes	TLNS
011	NSU3D	N	UT12+	SA	Yes	No	TLNS
012.01	TAS	N	UH15	SA*	Yes	Yes	
012.02	UPACS	C	SX11	SA*	Yes	No	
013.01	CFD++	C	UT5	SA	Yes	No	used node-centered grids
013.02	CFD++	C	UT5	KE*	Yes	No	used node-centered grids
013.03	CFD++	C	UX9	KE*	Yes	No	
014.01	OVERFLOW	N	SX3	SA*	Yes	Yes	Roe
014.02	OVERFLOW	N	SX3	SA*	No	No	HLLC, limited config 8
014.03	OVERFLOW	N	SX3	SA*	No#	No	Central, no grid study, no config 8
014.04	OVERFLOW	N	SX3	SST	No	Yes	Roe, no config 8
014.05	OVERFLOW	N	SX3	SA	No#	No	Roe, only one condition run
015	USM3D	C	UT4	SA	Yes	No	
016	FUN3D	N	UT5	SA	Yes	No	
017.01	FUN3D	N	UH6	SA	Yes	No	
017.02	CFL3D	C	SX1	SST	Yes	No	TLNS
017.03	CFL3D	C	SX1	SA	Yes	No	TLNS
017.04	CFL3D	C	SX2	SST	Yes	No	TLNS
017.05	CFL3D	C	SX1	SA	Yes	No	
018	ELSA	C	SX1	SA	Yes	No	
019	NSMB	C	SX10	SST	Yes	No	
020.01	USM3D	C	UT4	KO	No	No	no fine grid
020.02	USM3D	C	UT4	KO*	Yes	No	
021.01	NSU3D	N	UH6	SA	Yes	No	TLNS
021.02	NSU3D	N	UH6	SST	No	No	TLNS, no grid study

* = variant or special version
+ = merged and run by participant as a hybrid grid (B.L. tetrahedra merged into prisms)
# = very limited study; not included in statistical analysis
TLNS = full Navier-Stokes (N-S) with viscous cross-derivative terms neglected

term in SA to decrease dissipation within vortices; entries 013.02 and 013.03 used the k-ε-R_t version of the k-ε model; and entry 020.02 used a so-called "M1" modification to the Wilcox k-ω model. The interested reader is referred to the participant presentations posted on the HiLiftPW-1 website for more information.

Some key notes are also provided in Table 1. In spite of the fact that "fully turbulent" runs were requested (i.e., turbulence modeling active everywhere with no transition modeling), entries 001 and 009 utilized transition modeling/specification in their results. Entry 003.02 was a special set of three runs at $\alpha = 13^\circ$, 21°, and 28° on a set of grids specifically constructed for the purpose of comparing to entry 003.01 computations with support brackets, in order to obtain bracket increments. Entry 003.03 was a special grid convergence study for configuration 8 at $\alpha = 13^\circ$. Entries 013.01 and 013.02 were run using a cell-centered code, but utilized tetrahedral grids intended for node-centered codes. Thus, these runs achieved greater resolutions than node-centered codes running on the same set of grids. Entries 014.01 - 014.03 explored the effect of various flux constructions (Roe's flux difference splitting, HLLC flux splitting, and central differencing). Finally, some of the entries neglected the cross-derivative viscous terms. This is sometimes referred to as a "thin-layer Navier-Stokes" approximation (TLNS). For CFL3D, a subsequent entry also explored the effect of this approximation by running full Navier-Stokes (entry 017.05). For the unstructured code NSU3D, by default the Navier-Stokes viscous terms are taken as $\mu\nabla^2 v$, where μ is the viscosity and v denotes the velocity vector. In this form the Laplacian of the velocity can be computed in a single edge-base loop over all elements. Note that this form of the viscous terms corresponds to the incompressible Navier-Stokes formulation. The unstructured code EDGE contains a similar thin-layer type of formulation for which only normal derivatives are included.[9] Both of these unstructured codes also have an option for discretizing the full Navier-Stokes terms, but this option was not employed for the results submitted to the workshop.

Table 2 summarizes the grid systems used by participants of the workshop. The top half of the table lists nine of the ten grids supplied by the HiLiftPW-1 committee prior to the workshop (one grid, an unstructured hexahedral version of Str-OnetoOne-B, was not used by any participant and so is not listed here). As noted in Table 1, 32 of the 39 entries used committee-supplied grids. The bottom half of the table lists the grids created by participants. All of these grids except the Cartesian-based CB16 were made available on the HiLiftPW-1 website after the workshop. In the table, "Struct" stands for structured grid and "Unstr" stands for unstructured. "Tet" refers to tetrahedral elements, "Hex" to hexahedral elements, and "Mixed" to mixed elements. The number of nodes/cells are listed for the configuration 1 grids only, in order to give a general idea about the grid sizes. Nodes correspond to grid points and cells correspond to grid elements or volumes. Voxels in the Cartesian-based grids (for use with Lattice-Boltzmann) are similar to cells. Note that in addition to the required fine (F), medium (M), and coarse (C) grid levels (as defined on the HiLiftPW-1 website), in some cases extra fine (XF) and extra coarse (XC) grids were made available. Additional details about the grids can be found in Slotnick et al.[8] or on the website. Note that grid system UH6 is the same as UT5 with boundary-layer tetrahedra merged into prisms. Also, grid system UX9 is identical to SX1 translated into unstructured hexahedral elements.

Participants were allowed to add, modify, or remove their submissions in the 2 months following the workshop. A summary of the changes is provided in Table 3.

III. Lift Curve and Polar Comparisons

Fig. 2 gives an overall picture of the collective results (excluding entries 003.03 and 014.05) for configuration 1, over the range of angles of attack from $\alpha = 6^\circ$ to 37°. Results from CFD entries are indicated by red lines, while experimental data are shown with blue dots. There were several CFD outliers (defined loosely here as results that did not fall in the range of most of the other CFD results), especially at the higher angles of attack. The outliers will be quantified in greater detail in the Statistical Analysis section below. Lower and upper experimental bounds were estimated based on data from three different test campaigns,[8] and are indicated in the figure by solid blue lines. Overall, as a group, it appeared that CFD tended to under-predict lift, drag, and magnitude of the moment (moment was negative) compared to experiment.

Note that all results except entry 009 were on medium-level grids. Entry 009 only supplied polar results on a fine grid. In the section on Grid Convergence Behavior, the effect of grid density on forces and moment will be shown. It is also important to note that none of the CFD results in Fig. 2 included support brackets. The effects of the brackets on the CFD solutions will be shown in a later section.

The predictions at $C_{L,\max}$ are analyzed in more detail in Fig. 3. Here, results are differentiated by turbulence model. Note that aberrant results from entries 008.01, 008.02, and 008.03 (discussed in the next section) were not included. Most entries did a reasonably good job predicting both $C_{L,\max}$ (near 3.0) and the angle of attack at which it occurred (near 33°). As a group, the entries that employed the SA turbulence model tended to predict higher $C_{L,\max}$

Table 2. Summary of grids

Grid	Type	ID on website	Brackets?	Nodes/cells (millions)
SX1	Struct	Str-OnetoOne-A	No	F:171/161, M:52/48, C:23/20, XC:7/6
SX2	Struct	Str-OnetoOne-B	No	F:85/81, M:29/27, C:11/10, XC:4/3
SX3	Struct	Str-Overset-A	Yes	XF:282, F:83, M:25, C:11 (nodes)
UT4	Unstr Tet	Unst-Tet-Cellcentered-A	No	F:11/63, M:4/22, C:1/7
UT5	Unstr Tet	Unst-Tet-Nodecentered-A	No	F:32/190, M:11/64, C:4/21
UH6	Unstr Hybrid	Unst-Mixed-FromTet-Nodecentered-A	No	F:32/127, M:11/38, C:4/10
UH7	Unstr Hybrid	Unst-Mixed-Nodecentered-A	No	M:31/79, C:16/44, XC:13/37
UH8	Unstr Hybrid	Unst-Mixed-Nodecentered-B	Yes	F:111/141, M:37/49, C:12/17
UX9	Unstr Hex	Unst-Hex-FromOnetoOne-A	No	F:162/161, M:48/48, C:20/20, XC:6/6
SX10	Struct	Str-OnetoOne-D	No	F:48, M:20, C:6 (cells)
SX11	Struct	Str-OnetoOne-E	No	F:130/124, M:39/37, C:13/11
UT12	Unstr Tet	Unst-Tet-Nodecentered-B	No	F:31/185, M:10/59, C:4/21
UH13	Unstr Hybrid	Unst-Mixed-Cellcentered-A	No	F:92, M:31, C:11 (cells)
UH14	Unstr Hybrid	Unst-Mixed-Cellcentered-B	No	F:22/63, M:8/22, C:3/8
UH15	Unstr Hybrid	Unst-Mixed-Nodecentered-C	Yes	F:72/203, M:28/81, C:12/35
CB16	Cartesian-based	N/A (Lattice-Boltzmann only)	Yes	F:193, M:101, C:62 (voxels)

Table 3. Summary of changes in entries (post-workshop)

Entry	Change
001	updates of XC and some M results
002	new (replaced) submission on new grids
007	updates of configuration 8 results for $\alpha \geq 28$
009	redefined C as M, M as F, and added new C results
010	corrections to wing-only forces
012.01	new (replaced) submission on new grids
014.01	expanded results, added bracket computations
014.04	new submission
014.05	new submission
017.05	new submission
019	updated some results and made corrections to skin friction data

(in better agreement with experiment) than other turbulence models. However, there was not a clear trend exhibited for the angle of attack at $C_{L,\max}$ by turbulence model type.

IV. Grid Convergence Behavior

In Fig. 4, moment polars are shown by grid type for both coarse and fine grids. On coarse grids (Fig. 4(a) and (b)), the unstructured grid type exhibited greater variability than the structured type. However, on the fine grids (Fig. 4(c) and (d)), the variability between structured and unstructured grids was similar. These figures show SA results as red squares and all other models as black triangles. Generally, on the fine grid the SA results tended to be closer to experiment than the non-SA results.

Fig. 5 shows grid convergence results for configuration 1 at $\alpha = 13°$. N is the number of grid points or cells. $N^{-2/3}$ represents an effective grid spacing squared. If a code is converging as second order, the curve will be a straight line. Separate plots are presented for structured and unstructured grids, and within each plot the SA results are plotted with red lines and other turbulence models are plotted with black lines. (Note that the Lattice-Boltzmann result from entry 009 was included here as an unstructured code.) Experimental results, linearly interpolated from the data to the specific angle of attack, are displayed as a blue dot on the y-axis. Several apparent outliers are identified in the plots. Many of these were consistently different from the collective. One, entry 003.01, strayed from the collective only on the XF grid level. This aberrant behavior also occurred for entries 003.01 and 003.03 on the XF grid at other conditions, to be shown below.

It appears that with structured grids (plots on the left half of the page) many of the non-SA models were tending toward different solutions (lower lift, lower drag, lower magnitude moment) than SA. However, with unstructured grids (plots on the right half of the page) there was no clear trend with turbulence model. Overall with both structured and unstructured grids, the lift tended to increase with increasing grid refinement (in better agreement with experiment), and the magnitude of the moment tended to increase (in better agreement with experiment). There was not an overall clear trend in drag with increasing grid refinement. Also, from these plots it is apparent that many of the coarse unstructured grids tended to be coarser than their coarse structured counterparts (note that the single structured point with $N^{-2/3} > 4 \times 10^{-5}$ was an additional XC grid, beyond the F-M-C grids requested).

Fig. 6 shows grid convergence results for configuration 1 at $\alpha = 28°$. Generally, the same conclusions can be drawn at this angle of attack, although there was perhaps more of a noticeable increase of drag with grid refinement. In addition, several entries yielded results with unusually low lift compared to experiment and the collective CFD results. These aberrant entries were 003.01 (XF grid only), 008.01, 008.02, and 008.03. At the workshop, this issue was discussed extensively. These particular CFD results exhibited significant separation. Some other participants claimed that they had also experienced premature stall in their CFD solutions at high angles of attack when they did not restart from previously converged solutions at lower angles of attack. In other words, some participants noted initial condition dependency of their CFD solutions at high angles of attack.

V. Predicting ΔC_L Between Configurations

Fig. 7 shows lift curves for configurations 1 and 8, with separate plots for each of the 6 CFD codes with multiple submissions. Here, all turbulence model results were plotted together. Recall that some submissions were not complete; if a particular submission did not include complete configuration 8 results, then it was not plotted at all here. Overall, results from these 6 codes were consistent with each other at lower angles of attack, but at high angles of attack there was more variability between them. The correct trend of lower lift for configuration 8 prior to stall was predicted by all entries. In the experiment, the difference in C_L decreased with increasing angle of attack. In some cases a similar trend was seen in the CFD, while in others the difference did not appear to diminish as much.

Fig. 8 shows the configuration 1 and 8 results from the remaining CFD codes. In this case, all the results except for two were consistent with the previous figure. Entry 009 predicted somewhat higher C_L levels than the other codes, and generally lay at or above the experimental data. Part of this difference may have been due to the fact that entry 009 reported their polar data only on the fine grid. Also recall that entry 009 specified transition, which may have had some impact. The second set of results that was inconsistent with the others was entry 019, which yielded generally lower lift levels and much earlier stall.

The differences between the SA model and other models is explored in Fig. 9. As was also noted earlier from Fig. 3, the SA results generally yielded higher lift levels near stall, in better agreement with experiment than other models. Two of the "other models" that yielded higher lift levels were entries 001 (SST) and 009 (VLES) but both of these entries employed transition modeling/specification. It is possible that accounting for transition had an impact on

the predictions. The figure also points out some of the entries that predicted stall earlier than the collective: 005.02 for configuration 8, and 017.04 and 019 for both configurations.

The drag and moment deltas are not examined here. However, at the end of the Statistical Analysis section, plots will be given showing the trends for those quantities, in addition to lift.

VI. Surface Pressures and Skin Frictions

A tremendous amount of CFD data was collected from participants at the workshop. Among this data were surface pressure coefficients (mandatory) and surface skin friction coefficients (optional) along nine slat stations, nine wing stations, and eleven flap stations for all cases and grids computed. It is difficult to do more than present a very small sampling of these results. At present, results at only a few conditions and locations have been examined in any detail for configuration 1 at $\alpha = 13^\circ$ and 28°. These conditions were chosen because they were run using multiple grid sizes, making it possible to note trends with grid refinement. Here, we focus on only a few selected results that demonstrated some trends among the broader collective results. Note that lines are used when plotting the CFD pressure and skin friction data in the figures unless the participants submitted non-ordered data, in which case small symbols are used instead.

Fig. 10(a) shows the locations of the pressure stations to be shown in this and future figures, and Figs. 10(b) – (f) give the surface pressure coefficients on the flap for configuration 1 at $\alpha = 13^\circ$ along the 85% span station. Fig. 10(b) shows results from entry 009, which included transition. In this result, the pressures showed little difference between the medium and fine grids. The C_p levels on the upper surface indicated more suction than in the experiment. Although not shown, the other entry that accounted for transition (001) yielded similar over-prediction of upper surface suction.

Figs. 10(c) and (d) exhibit another trend seen among the collective results, that the SST model had more of a tendency to separate near the upper surface trailing edge of the flap. In these two figures, the same code and grid were used with SST and SA, respectively. The SST model produced less upper surface suction near the front of the flap, and separated near the trailing edge. The SA model yielded much closer agreement with experiment. In both of these structured-grid cases, there was very little sensitivity to grid density.

Figs. 10(e) and (f) demonstrate the increased grid sensitivity when using an unstructured tetrahedral grid (UT5) compared to the same grid with boundary layer tetrahedra merged into prisms (UH6). In both cases, the same CFD code was employed. The results on the fine grid were similar to each other, and agreed reasonably well with experiment. However, coarser tetrahedral grid results were worse than those on the coarser hybrid grid. These figures also demonstrate how some entries, even with the SA model, yielded poor agreement with experimental pressure data near the trailing edge of the flap upper surface.

A sampling of x-component of surface skin friction coefficients at the same conditions and same flap location as Fig. 10 is shown in Fig. 11. Only a few results were chosen to illustrate specific observations. Recall that reporting skin friction was optional; 14 of the 39 entries did not report it. Fig. 11(a) shows entry 007, a result typical of many entries. In this case there was very little grid sensitivity (although not shown, entries 015, 016, 020.01, 020.02, and 021.02 exhibited the largest grid sensitivity of those who reported it). Entry 007 also shows upper surface separation on the flap very near the trailing edge. Most entries yielded either incipient or various degrees of flap trailing edge separation. Entry 001, which utilized a transition model, produced very different skin friction data on the flap. In Fig. 11(b), it is seen that the flow exhibited apparent transition to turbulent flow near $x = 73$ on the flap upper surface.

Figs. 11(c) and (d) exhibit the effect of a particular variant of the SA turbulence model. In entry 014.01, the SA-fv3 variant of the SA model was used, which is known to delay the onset of full turbulence in some circumstances.[10] Fig. 11(c) exhibits an apparent transition to turbulence between $x = 70$ and 71. This delayed onset of turbulence was eliminated in entry 014.05, which used the standard SA model.

Figs. 11(e) and (f) show two entries that produced unusual skin friction behavior compared to the others. Entry 012.01 yielded oscillatory behavior near the upper surface leading edge, but otherwise appeared normal. Entries 021.01 (in Fig. 11(f)) and 021.02 (not shown) were the only entries that did not indicate incipient or actual trailing edge separation in their skin friction.

In order to get an idea of the consistency of CFD results when using a specific turbulence model, C_p plots are given for the SA model only in Figs. 12 - 15. Fine grid results on all three elements are shown at two span stations of 28% and 85% and at two angles of attack of $\alpha = 13^\circ$ and 28°. Furthermore, the plots are divided into structured grid results (blue lines) and unstructured grid results (red lines). There are seven structured entries plotted (003.01, 012.02, 014.01, 014.02, 017.03, 017.05, and 018) representing four different codes and twelve unstructured entries plotted (004, 005.01, 006, 007, 010, 011, 012.01, 013.01, 015, 016, 017.01, and 021.01) representing eight different codes. On the slat and main elements at these span stations, other than a few individual outliers, most CFD results were very

consistent with each other and agreed well with experimental data. On the flap element, however, there tended to be greater variation at the 85% span location, particularly near its trailing edge.

The flow field very near the wing tip turned out to be very difficult to predict. Here, we turn our attention to configuration 1 at $\alpha = 28^\circ$. At the wing tip location (98% span), submitted results varied widely, with some agreeing with experimental data fairly well and some very poorly. Fig. 16 shows results from two different entries. Entry 018 (on the left) was one of the entries that agreed best with the data (although it still missed levels on the flap upper surface and near the trailing edge of the main element), while entry 010 (on the right) was typical of many entries that did not agree well on the main and flap elements. The reasons for the wide variance in the wing tip region among participants is not completely known, but there were at least some characteristics identified that had a large impact, as will be shown in the next figure. In particular, a wing tip vortex forms and rolls up over the elements; the success in accurately capturing this vortex no doubt plays an important factor in the ability to predict the surface pressures there.

Another good way to visualize the ability of CFD to predict the tip region is via the spanwise flap stations. For example, in Fig. 17 sample surface pressure coefficients along the forward spanwise flap station are shown (for configuration 1 at $\alpha = 28^\circ$, identified by flapfwdspan in Fig. 10(a)). Fig. 17(a) shows a typical full Navier-Stokes result. In this entry, there was very high sensitivity to grid density in the outboard region. As the grid was refined, the pressures near the wing tip got better compared to experimental data, but even on the fine grid the results near the wing tip were not very good (too low suction). All entries except one (009) predicted too-low suction at the wing tip. The entry 009 result (shown later in the Effects of Brackets section) actually predicted *too much* suction on the fine grid. The CFD data in Figs. 17(a) and (b) came from the same code, but employed a different grid. Both entries 013.02 and 002 used a form of the k-ε model, but it is not clear exactly how they differed (entry 013.02 used a k-ε-R_t model, and 002 used a preconditioned realizable k-ε model). The entry 002 result was poor in the outboard region even on the fine grid.

Figs. 17(c) and (d) illustrate the effect of neglecting the viscous cross-derivative terms on the flow near the wing tip. The only difference between entries 017.03 and 017.05 was the fact that the cross-derivative terms were neglected in entry 017.03. Full Navier-Stokes was employed for entry 017.05. The tip region results for entry 017.05 were dramatically improved. The entry 017.03 result was typical of others who neglected the viscous cross-derivative terms (entries 005.02, 010, 011, 017.02, 017.04, 021.01, and 021.02). This was a very important outcome of the workshop: the discovery of the large negative impact of neglecting viscous cross-derivatives on the flow near the wing tip.

Finally, Figs. 17(e) and (f) illustrate an effect of turbulence model on the wing tip region. Here, the only difference between entries 015 and 020.02 was the turbulence model (SA vs. a modified k-ω). The SA result agreed better with the experimental data near the wing tip.

In Fig. 17, one can see a few dips in the experimental pressure data that are not predicted by any of the CFD methods. It turns out that these dips were caused by the presence of the support brackets. In the next section, the CFD entries that included brackets are assessed.

VII. Effects of Support Brackets

The general effects of including support brackets on the forces and moment are shown in Fig. 18. Here, all CFD results were on medium grids except for one (entry 009, which used fine). The experimental bounds[8] are indicated by dashed lines in the figure. The CFD trend with brackets was to yield a small drop in lift at $\alpha = 13^\circ$ of about $0.01 - 0.02$ and a larger drop at $\alpha = 28^\circ$ of about $0.06 - 0.09$. Note that one entry (014.04) stalled too early, so its $\alpha = 28^\circ$ result with brackets was not realistic. The trend for drag at $\alpha = 13^\circ$ was not as clear: for five entries the drag increased and for two entries it decreased. However, at $\alpha = 28^\circ$ the brackets yielded lower drag for all entries. Moment generally decreased in magnitude (became less negative) with the addition of brackets.

Two locations where the support brackets influence on the surface pressure coefficients could be seen were at the 50% flap span station and on the flap forward span station. Fig. 19 shows a sampling of results for three of the entries that included brackets. At the 50% flap span station (left three plots in the figure), when brackets were not included, most entries produced upper surface C_p with greater suction over the forward part of the flap than the experiment, and less flatness over the rear part. In these cases, the CFD result with brackets agreed much better with experimental data. On the other hand, the entry 009 results without and with brackets yielded very little difference. The reason for the different behavior of entry 009 at the 50% flap span station is not known.

At the flap forward span station (right three plots in the figure), including support brackets in the CFD computation yielded results that followed the dips in the experimental data, although the levels did not always agree well with experiment. Fig. 19(f) also illustrates how entry 009 over-predicted the suction near the wing tip on the fine grid. As mentioned earlier, this result was very different from all other CFD entries.

VIII. Statistical Analysis

In the statistical analysis, the basic method used by Morrison[11] for the DPW analysis was adopted. For any quantity of interest (C_L for example), the scatter limits are established as $\hat{\mu} \pm K\hat{\sigma}$, where $\hat{\mu}$ is the median of the sorted data, $\hat{\sigma}$ is the standard deviation, and K is a confidence interval coverage factor, taken to be $K = \sqrt{3}$. However, note that this value of K is not standard. Hemsch and Morrison[12] used a more conservative value of $K = 3$. A statistical outlier (a point residing outside of the scatter limits) is by definition different from the results that lie within the scatter limits. In terms of CFD solutions, being an outlier means that some aspect of the CFD solution was significantly different from the others, and its cause(s) should be investigated. In the plots to follow, any sample lying outside of the limits is noted in the figure. However, because the scatter limits depend on the choice of K, the fact that a particular point lies outside may or may not be significant. For example, if $K = 3$ had been chosen instead of $K = \sqrt{3}$, then many of the tagged points would have resided within the scatter limits. Therefore, the plots to follow should be used only as a crude indication of potentially significant CFD differences.

The coefficient of variation, defined as $C_\nu = \hat{\sigma}/\hat{\mu}$, provides a measure to compare the variation of populations with different medians. Recall that the entries 003.02, 003.03, 014.03, and 014.05 were special CFD cases with only very limited numbers of runs completed. Therefore, these four entries were not included in the statistical analysis.

Fig. 20 shows the C_L, C_D, and C_M for all entries at $\alpha = 13°$, as well as the median, scatter limits, and coefficients of variation. The scatter limits are shown as dashed lines in the plots. For all three quantities, the scatter and coefficient of variation decreased in magnitude as the grid was refined. On the fine grid level, the scatter in C_L was 0.10, the scatter in C_D was 232 counts (0.0232), and the scatter in C_M was 0.052. It can be argued that comparing CFD results with different turbulence models is not appropriate, because different equations are being solved. Therefore, Fig. 21 shows a statistical analysis of only those entries that used some version of the SA model. Note that by limiting the statistical analysis to SA only, the scatter and coefficients of variation decreased substantially from Fig. 20. On the fine grid level, the scatter in C_L was 0.06, the scatter in C_D was 136 counts (0.0136), and the scatter in C_M was 0.020.

Statistical analysis results for $\alpha = 28°$ are shown in Fig. 22. Because of the recognized aberrant behavior of entries 008.01, 008.02, and 008.03 at $\alpha = 28°$ (see discussion in the Grid Convergence Behavior section), these particular entries were omitted from the statistical analysis at this angle of attack. In this case, again the scatter and coefficient of variation decreased in magnitude as the grid was refined. Fig. 23 shows $\alpha = 28°$ results using SA only. As with the $\alpha = 13°$ case, limiting the statistical analysis to SA significantly reduced both the scatter and coefficients of variation. On the fine grid level, the scatter in C_L was 0.07, the scatter in C_D was 291 counts (0.0291), and the scatter in C_M was 0.042. It is interesting to note that the C_ν values for lift and drag when looking only at SA results were about the same ($C_{\nu,\text{lift}} \approx 0.007$, $C_{\nu,\text{drag}} = 0.012$) for both angles of attack on the fine grids. However, the C_ν for moment more than doubled from $C_{\nu,\text{moment}} = -0.012$ to -0.027.

Statistical analyses were performed for the configuration 8 results (submitted by participants on the medium grid level only), but are not shown here. Results were generally similar to results for configuration 1. Again, limiting the procedure to SA typically reduced both the scatter and coefficients of variation.

Finally, grid convergence plots including scatter limits are shown in Figs. 24 and 25. Entries are shown for configuration 1 (in red) only if both configurations 1 and 8 were submitted. The blue solid line represents the median for configuration 1 at the C-M-F grid levels, and the blue dashed lines represent the scatter limits for configuration 1. Because configuration 8 was only computed on medium grids, the entries themselves are not plotted, with the one exception of special entry 003.03, which performed a grid study for configuration 8 at $\alpha = 13°$. Note the aberrant behavior discussed earlier for entry 003.01 on the XF grid also occurred for entry 003.03. The median and scatter limits for the configuration 8 medium grids are shown in green. The filled-in symbols on the y-axis represent experimentally measured values interpolated to the specific angle of attack. Open symbols for configuration 1 represent estimated experimental bounds.[8] Similar experimental bounds were not available for configuration 8. The delta values on the medium grid between configurations 1 and 8 are also indicated, in text, in the upper left hand corner of each plot.

For $\alpha = 13°$, the configuration 1 CFD scatter limits for all forces and moments were similar in extent to the experimental error bounds, but CFD somewhat under-predicted C_L, C_D, and the magnitude of C_M. When using only SA results, the scatter limits and convergence were much tighter than when considering all turbulence model results. For $\alpha = 28°$, similar trends were seen, except that all forces and moments appeared to be converging (in the mean) closer to the experimentally measured values as the grids were refined. It is difficult to draw conclusions regarding the trends for configuration 8 without a full set of entries on three sets of C-M-F grid levels. The current analysis only shows the differences on the medium grid. The ΔC_L, ΔC_D, and $|\Delta C_M|$ were all under-predicted in the mean by CFD at $\alpha = 13°$ by between 4 and 15%, and were all over-predicted at $\alpha = 28°$ by between 62 and 154%.

IX. Conclusions

The entries from the first AIAA High Lift Prediction Workshop (HiLiftPW-1) have been collectively summarized, both by looking at specific results compared to experiment as well as through statistical analyses. A large number of surface pressures and (optional) skin friction data were collected, but only a small portion of these have been analyzed to date. Additional analyses on these data can be conducted in the future.

In general, CFD tended to under-predict lift, drag, and the magnitude of the moment (moment was negative) compared to experiment. Predicting the flow was more difficult at higher angles of attack nearing stall; there was more spread among the solutions there, and some participants predicted early stall. At the workshop, some participants reported initial condition dependency of their CFD solutions at high angles of attack. Unless a high angle of attack solution was initiated with a converged flowfield obtained at a lower angle of attack, sometimes massive separation could result. This dependency may have been one of the reasons for some of the very poor results at high angle of attack. Also, some turbulence models appeared to do worse than others near $C_{L,\max}$. In spite of tending to predict lift somewhat too low in general, many participants were able to predict $C_{L,\max}$ and the angle of attack at which it occurred reasonably well.

The trends with grid refinement were generally in the correct direction (approaching experiment). For example, the lift coefficient for most entries increased as the grid was refined. However, it is difficult to draw firm conclusions regarding this comparison with experiment, because CFD grid convergence studies were only done without support brackets. Furthermore, by design this first workshop asked for CFD results with no transition modeling or tunnel walls, and these aspects may be important when comparing directly with the experiment. Regarding grid convergence, it appeared that unstructured type methods exhibited greater variability than structured methods on coarse grids, but on fine grids the variability was similar. Part of the difference in variability may have been the fact that the coarse unstructured grids tended to be smaller than the coarse structured grids. Collectively, the SA model yielded higher lift levels than other models near stall, in better agreement with experiment. Two exceptions to this trend were entries that also employed transition modeling or specification.

From the limited pressure and skin friction results analyzed, the following trends were observed. First, there tended to be greater variation among the CFD results at the outboard trailing edge region of the flap, and the SST model had a greater tendency to separate there than SA. Second, an unstructured tetrahedral grid was found to exhibit greater grid sensitivity than the same grid with its boundary layer tetrahedra merged into prisms. Third, the flowfield near the wing tip was very difficult to predict accurately: all entries except one seriously under-predicted the suction near the wing tip upper surface. Fourth, neglecting viscous cross-derivative terms yielded even worse predictions near the wing tip than full Navier-Stokes. Skin friction was also able to point out key differences between particular variants of the SA model, and could be used to easily see the influence of transition modeling.

The general effect of including support brackets was to decrease lift by a small amount at $\alpha = 13^\circ$ and a larger amount at $\alpha = 28^\circ$. The effects of brackets could be seen in the surface pressure data at certain stations. Grid studies were not performed for the bracketed configuration, so the trend with grid refinement is not known.

In the statistical analysis, scatter limits and coefficients of variation were computed. At both $\alpha = 13^\circ$ and 28°, the scatter and coefficients of variation both decreased in magnitude as the grid was refined. By limiting the analysis to only SA results, these levels decreased in magnitude substantially. Statistically, the predicted deltas between configuration 1 and 8 were somewhat low at $\alpha = 13^\circ$, and significantly high at $\alpha = 28^\circ$. A grid study is needed for configuration 8 to draw firmer conclusions.

Two of the recommendations to emerge from the workshop were: (1) collect iterative convergence histories to help assess convergence (or lack thereof), and (2) conduct additional grid studies with support brackets, on configuration 8, and near $C_{L,\max}$. Furthermore, in future workshops an effort should be made to try to reduce variability from the use of different versions of the same turbulence model, and from the use of numerical approximations such as neglecting viscous cross-derivative terms.

Regarding the six long-term goals for the HiLiftPW workshops stated in the introduction, this summary paper of the first workshop's results has primarily addressed the first (assessing the current prediction capability for these types of flows) and the fifth (providing an impartial forum for evaluation). It has also identified areas needing additional focus (the wing tip and the flap trailing edge regions), and has noted the potential importance of including support brackets as well as modeling transition. Many of the other goals are longer term, which future workshops and continued collaborative efforts will strive to address.

Acknowledgments

The work of the first author was supported under the Subsonic Fixed Wing Project of NASA's Fundamental Aerodynamics Program.

References

[1]Rumsey, C. L. and Ying, S. X., "Prediction of High Lift: Review of Present CFD Capability," *Prog. Aerospace Sciences*, Vol. 38, 2002, pp. 145–180.

[2]Nash, S. M. and Rogers, S. E., "Numerical Study of a Trapezoidal Wing High-Lift Configuration," SAE-1999-01-5559, October 1999.

[3]Johnson, P. L., Jones, K. M., and Madson, M. D., "Experimental Investigation of a Simplified 3D High Lift Configuration in Support of CFD Validation," AIAA Paper 2000-4217, August 2000.

[4]Rogers, S. E., Roth, K., and Nash, S. M., "Validation of Computed High-Lift Flows with Significant Wind-Tunnel Effects," *AIAA Journal*, Vol. 39, No. 10, 2001, pp. 1884–1892.

[5]Chaffin, M. S. and Pirzadeh, S., "Unstructured Navier-Stokes High-Lift Computations on a Trapezoidal Wing," AIAA Paper 2005-5084, June 2005.

[6]McGinley, C. B., Jenkins, L. N., Watson, R. D., and Bertelrud, A., "3-D High-Lift Flow Physics Experiment - Transition Measurements," AIAA Paper 2005-5148, June 2005.

[7]Vassberg, J. C., Tinoco, E. N., Mani, M., Brodersen, O. P., Eisfeld, B., Wahls, R. A., Morrison, J. H., Zickuhr, T., Laflin, K. R., Mavriplis, D. J., "Abridged Summary of the Third AIAA Computational Fluid Dynamics Drag Prediction Workshop," *Journal of Aircraft*, Vol. 45, No. 3, May-June 2008, pp. 781–798.

[8]Slotnick, J. P., Hannon, J. A., and Chaffin, M., "Overview of the 1st AIAA CFD High Lift Prediction Workshop," 49th AIAA Aerospace Sciences Meeting, American Institute of Aeronautics and Astronautics, Reston, VA (submitted for publication).

[9]Eliasson, P., "EDGE: A Navier-Stokes Solver for Unstructured Grids," FOI Report FOI-R-0298-SE, Swedish Defence Research Agency, ISSN 1650-1942, December 2001.

[10]Spalart, P. R., "Trends in Turbulence Treatments," AIAA Paper 2000-2306, June 2000.

[11]Morrison, J. H., "Statistical Analysis of CFD Solutions from the Fourth AIAA Drag Prediction Workshop," AIAA Paper 2010-4673, June-July 2010.

[12]Hemsch, M. J. and Morrison, J. H., "Statistical Analysis of CFD Solutions from 2nd Drag Prediction Workshop," AIAA Paper 2004-556, January, 2004.

Figure 1. Photograph of the Trapezoidal Wing in the NASA Langley 14x22 Foot Tunnel.

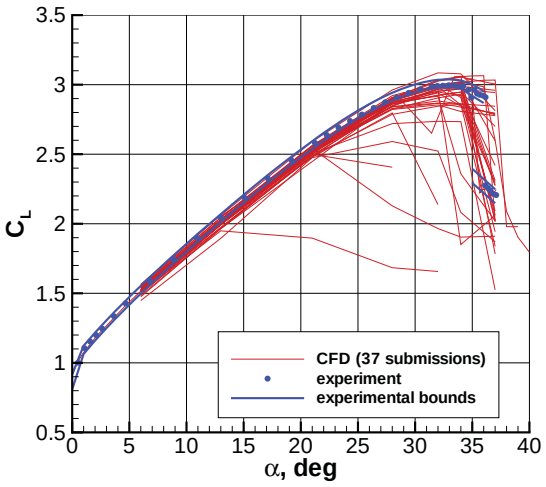

(a) Lift coefficient

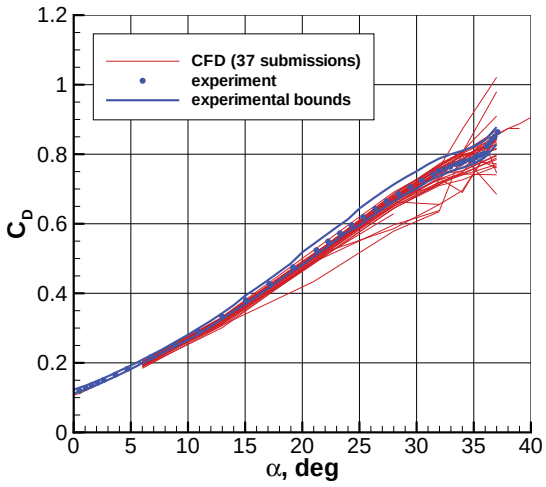

(b) Drag coefficient

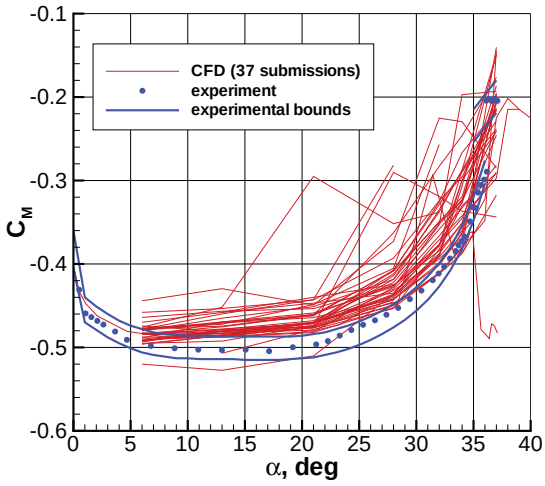

(c) Moment coefficient

Figure 2. Summary of all results for configuration 1, medium grids.

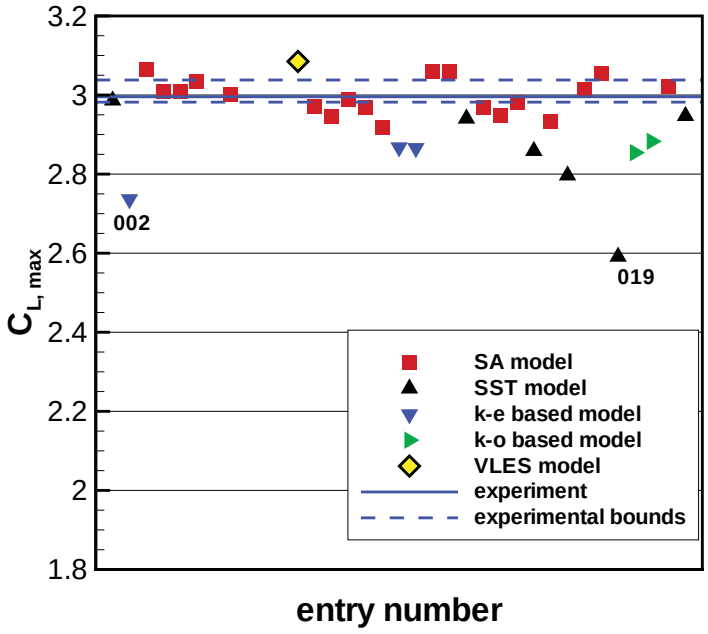

(a) $C_{L,\max}$

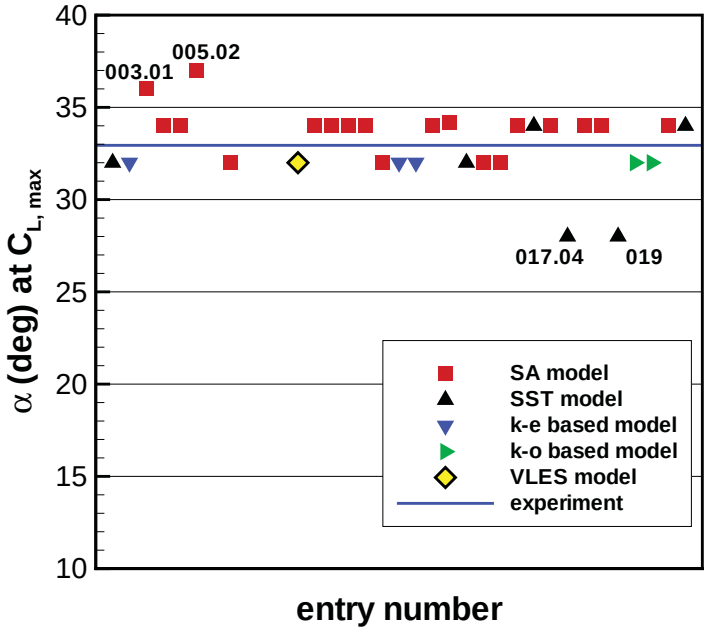

(b) Angle of attack at $C_{L,\max}$

Figure 3. Predictions of maximum lift for configuration 1, medium grids.

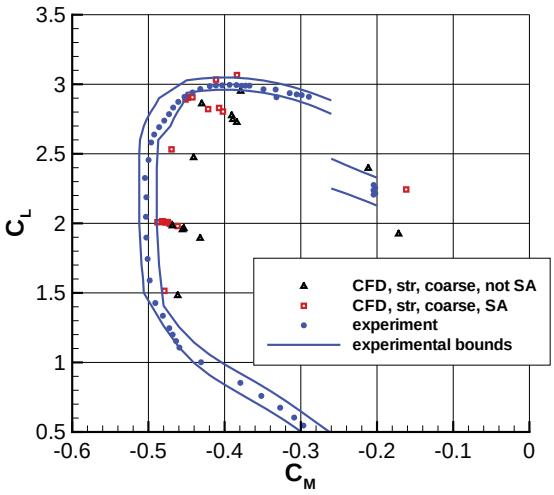

(a) Coarse grids, structured grids

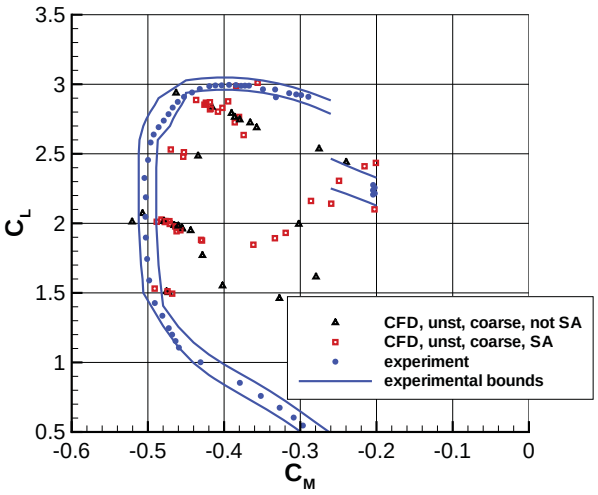

(b) Coarse grids, unstructured grids

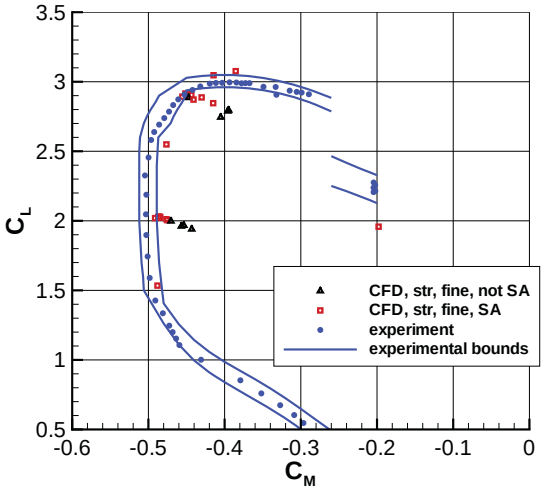

(c) Fine grids, structured grids

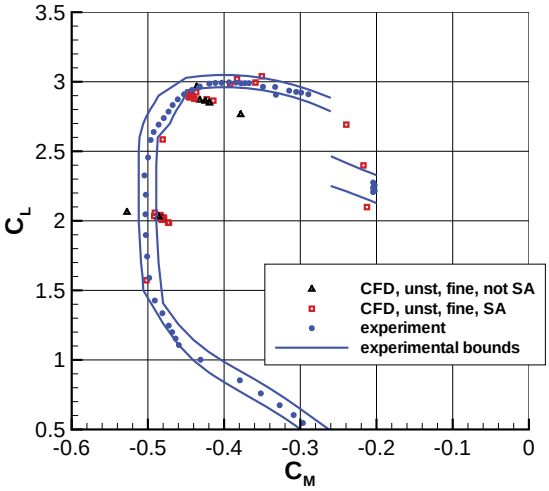

(d) Fine grids, unstructured grids

Figure 4. Moment polars for configuration 1.

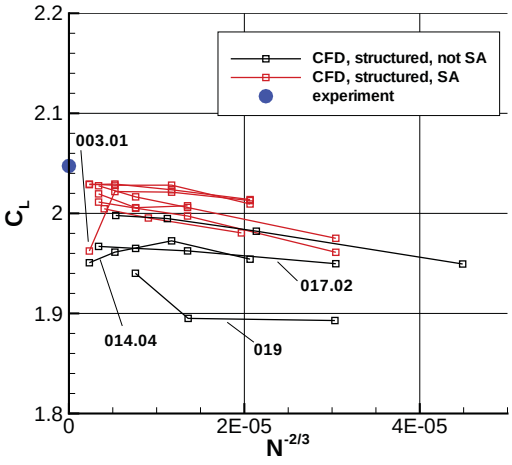

(a) Lift coefficient, structured grids

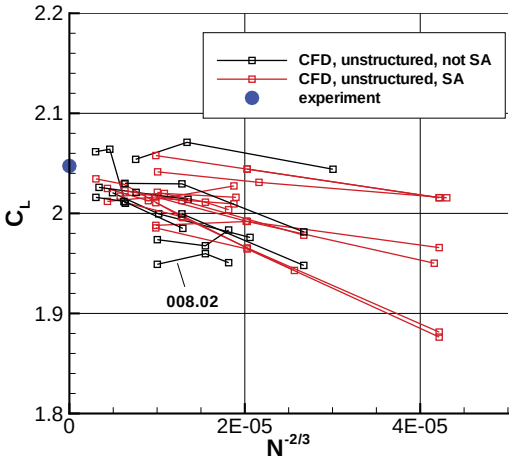

(b) Lift coefficient, unstructured grids

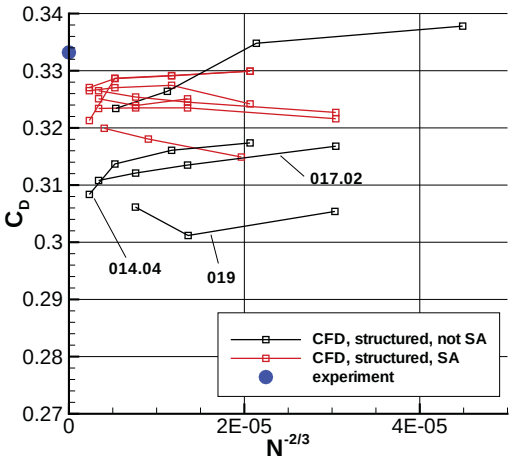

(c) Drag coefficient, structured grids

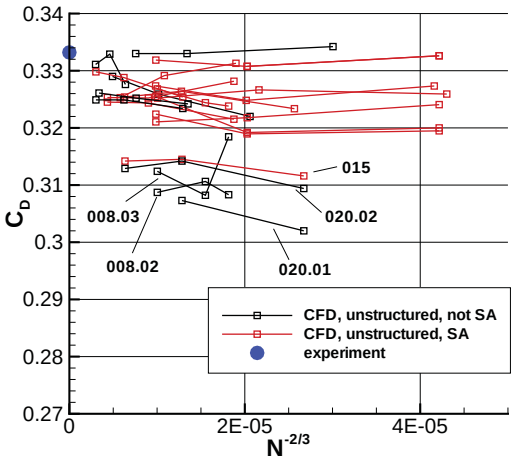

(d) Drag coefficient, unstructured grids

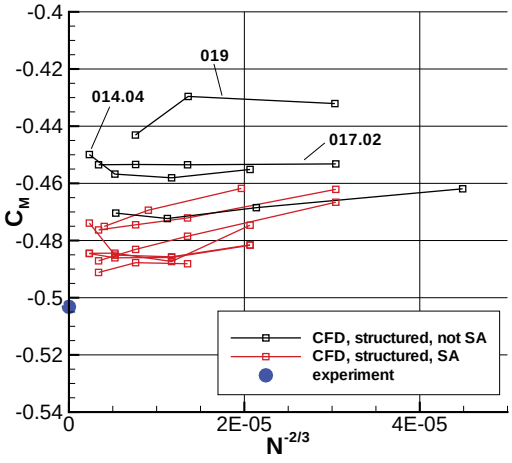

(e) Moment coefficient, structured grids

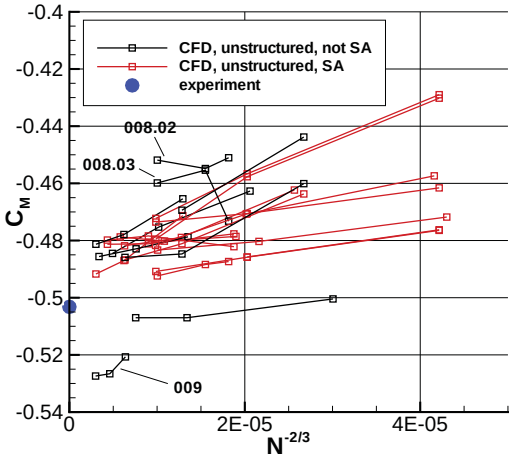

(f) Moment coefficient, unstructured grids

Figure 5. Grid convergence characteristics, configuration 1, $\alpha = 13°$.

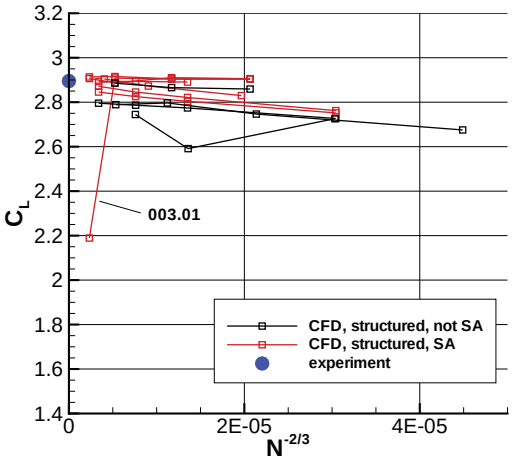

(a) Lift coefficient, structured grids

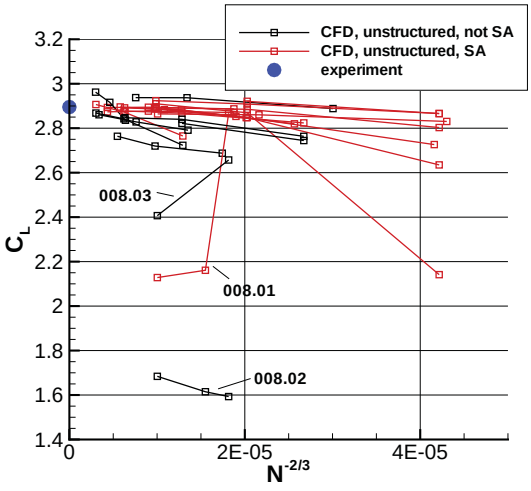

(b) Lift coefficient, unstructured grids

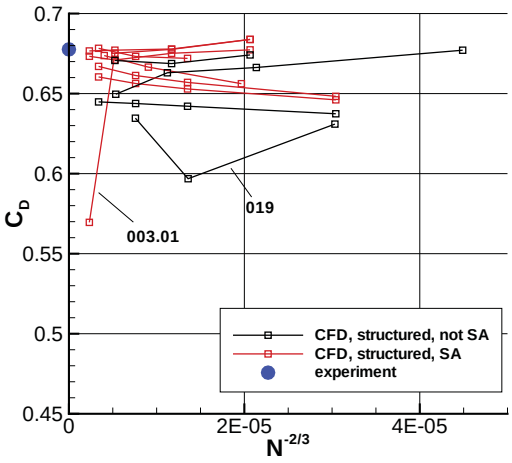

(c) Drag coefficient, structured grids

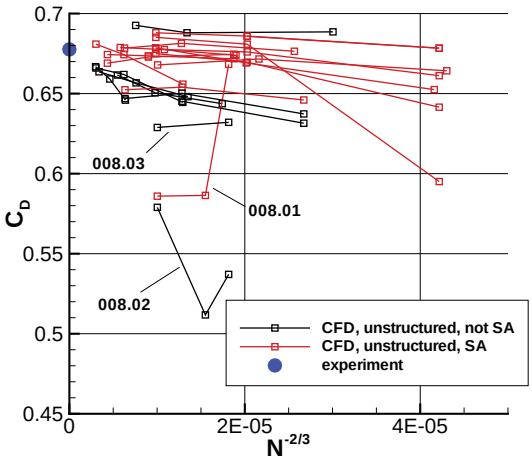

(d) Drag coefficient, unstructured grids

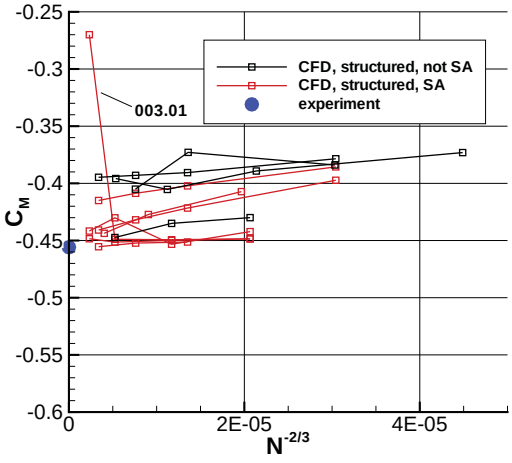

(e) Moment coefficient, structured grids

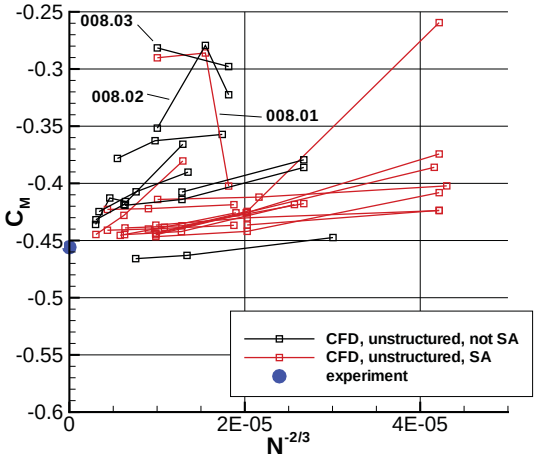

(f) Moment coefficient, unstructured grids

Figure 6. Grid convergence characteristics, configuration 1, $\alpha = 28°$.

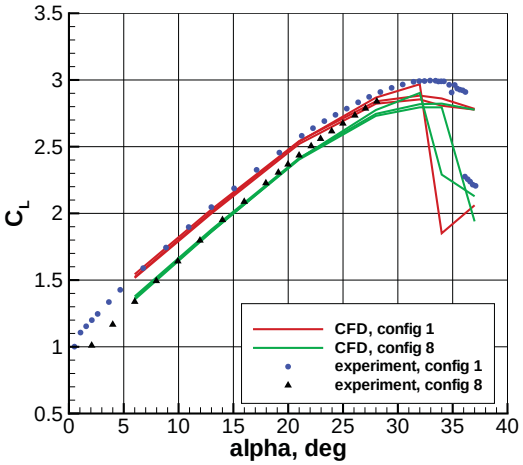

(a) USM3D

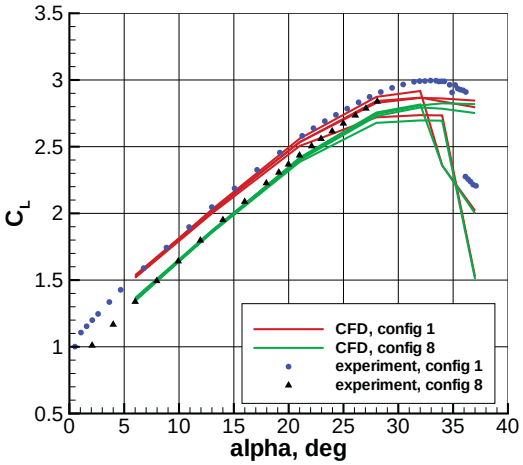

(b) CFD++

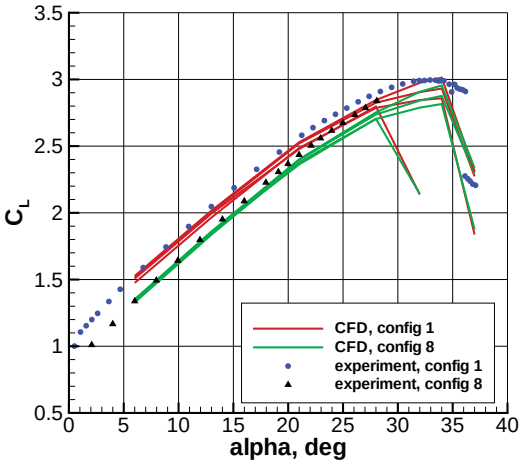

(c) CFL3D

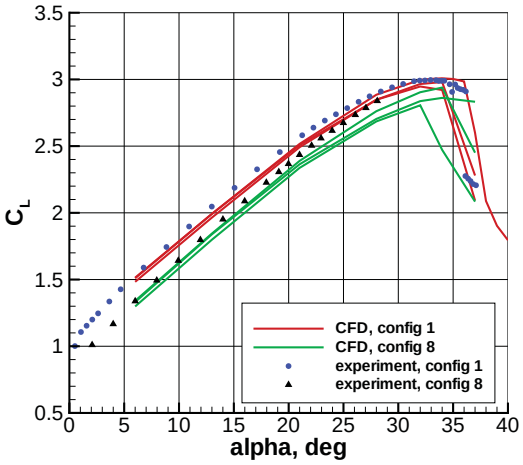

(d) FUN3D

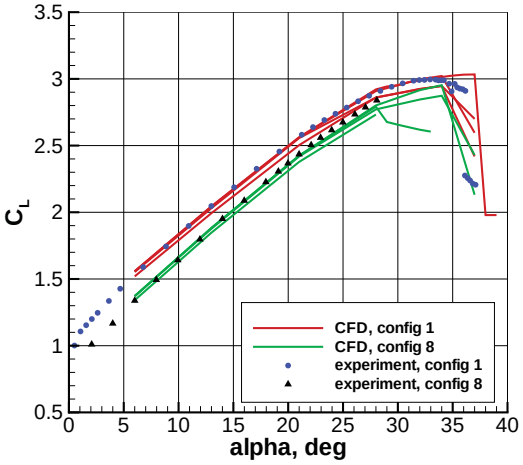

(e) NSU3D

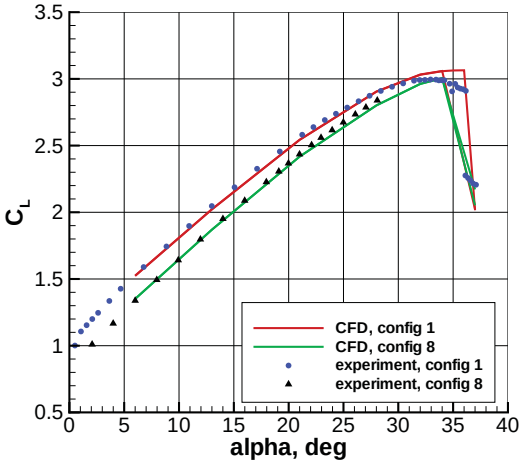

(f) OVERFLOW

Figure 7. Prediction of lift curve differences between configurations 1 and 8, by CFD codes with multiple submissions that computed both configurations, medium grids.

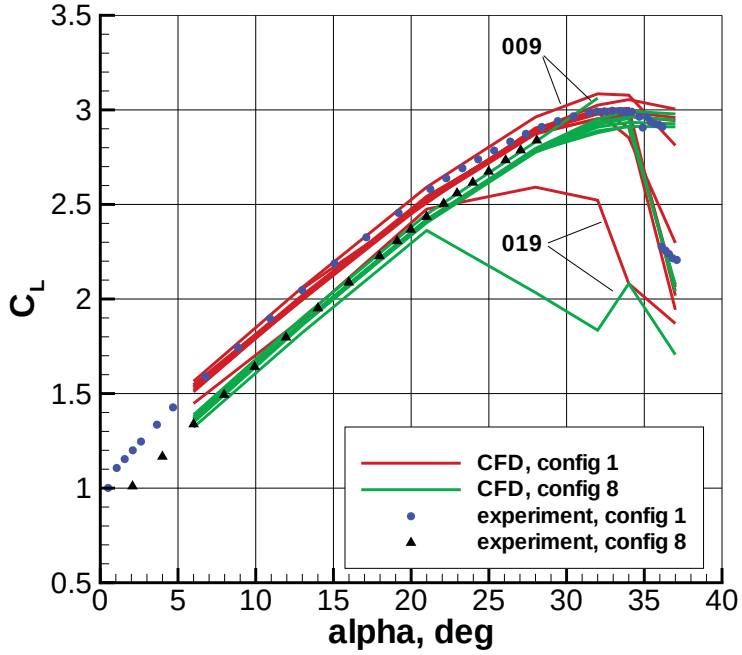

Figure 8. Predictions of lift curve differences between configurations 1 and 8, by CFD codes not included in Fig. 7 that computed both configurations, medium grids.

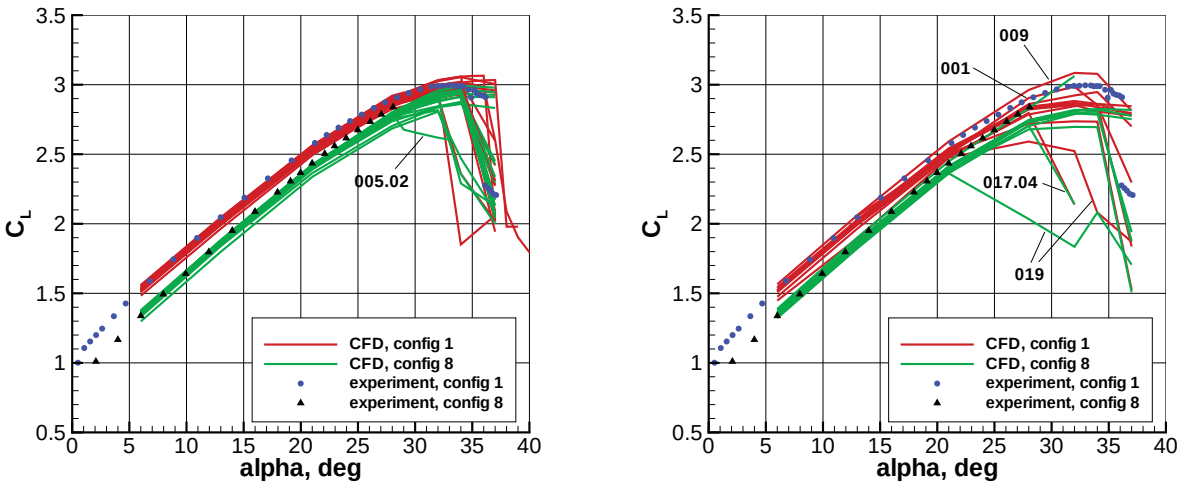

(a) SA model

(b) Other models

Figure 9. Prediction of lift curve differences between configurations 1 and 8, with SA model results separated out, medium grids.

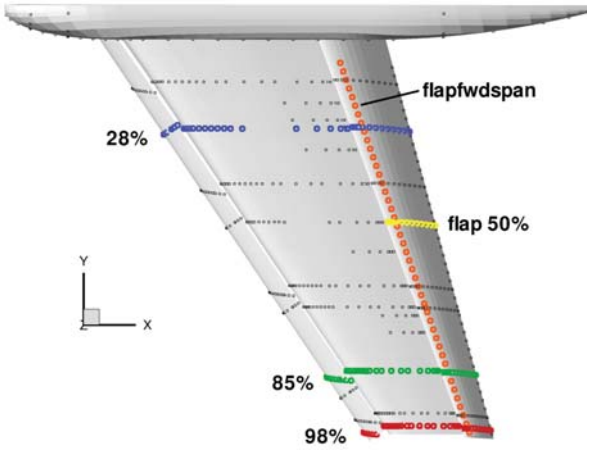

(a) Pressure tap locations

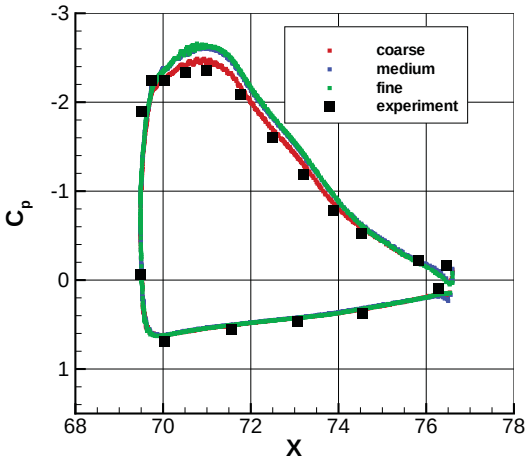

(b) Entry 009 (CB16 grid, VLES with transition)

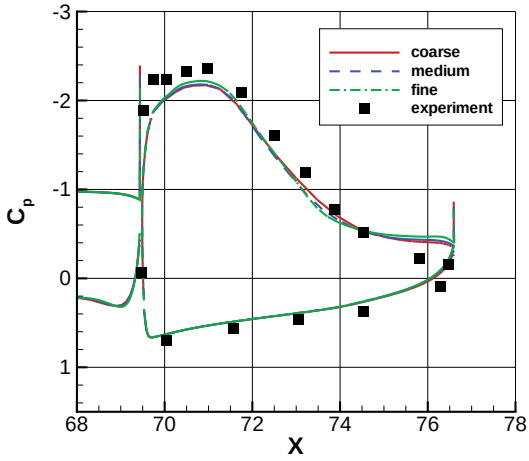

(c) Entry 017.02 (SX1 grid, SST)

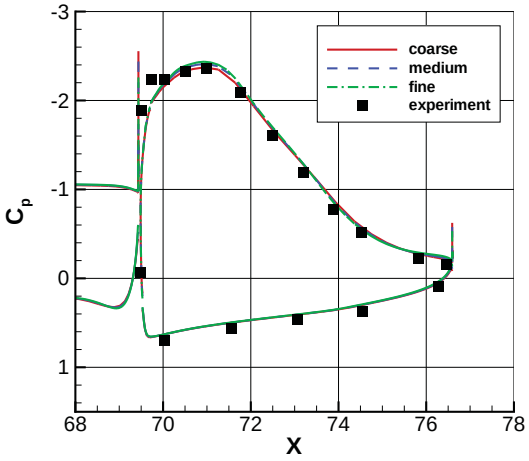

(d) Entry 017.03 (SX1 grid, SA)

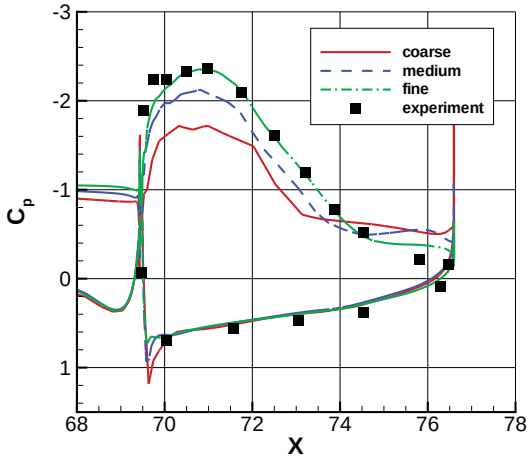

(e) Entry 016 (UT5 grid, SA)

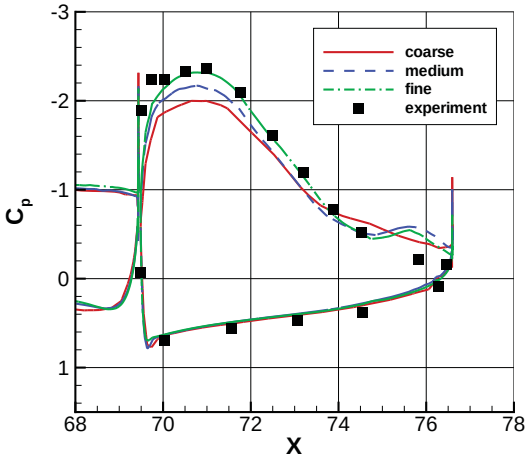

(f) Entry 017.01 (UH6 grid, SA)

Figure 10. Sampling of surface pressure coefficients at 85% flap station, configuration 1, $\alpha = 13°$ (experiment at $\alpha = 12.991°$).

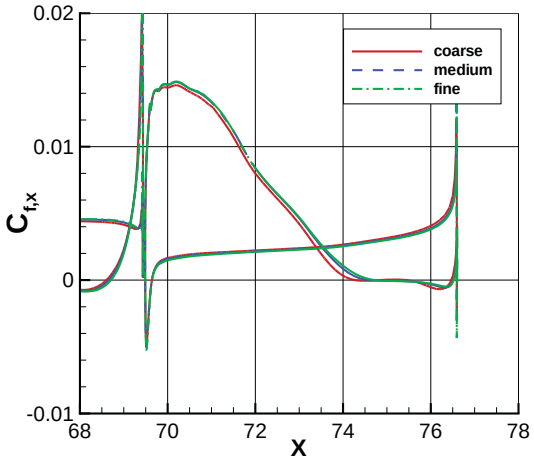

(a) Entry 007 (UH8 grid, SA)

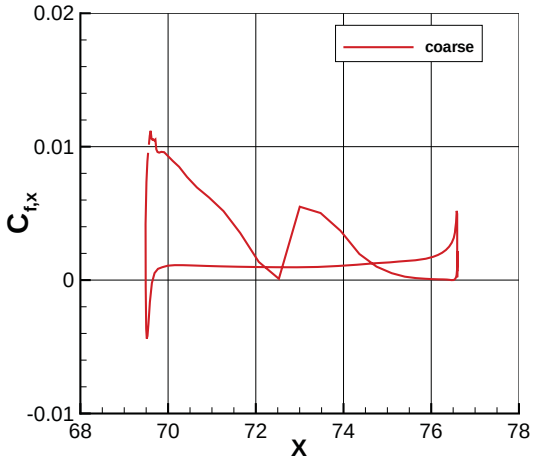

(b) Entry 001 (UX9 grid, SST with transition)

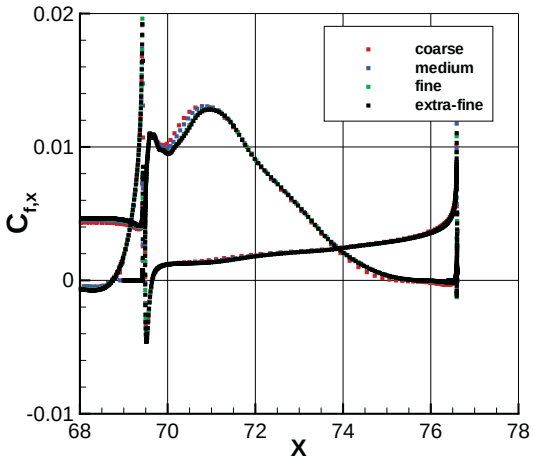

(c) Entry 014.01 (SX3 grid, SA*)

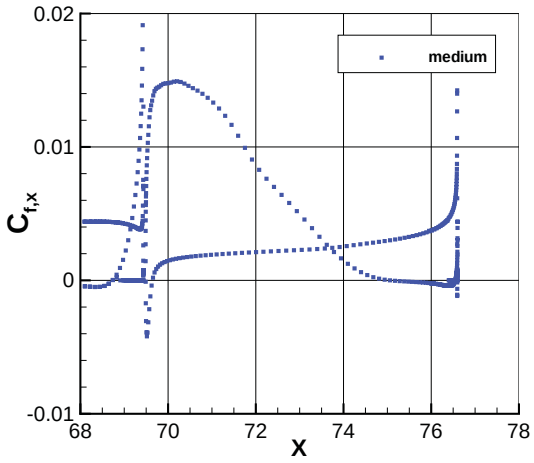

(d) Entry 014.05 (SX3 grid, SA)

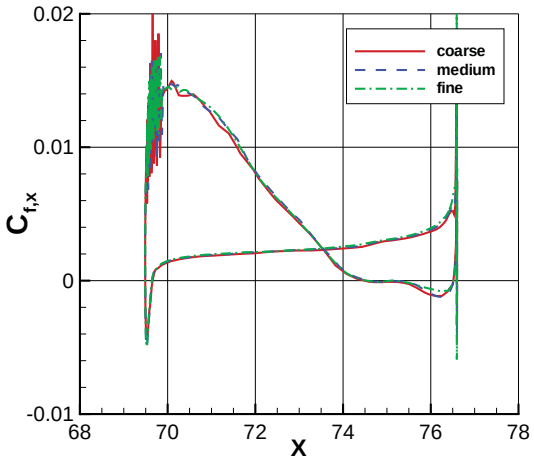

(e) Entry 012.01 (UH15 grid, SA*)

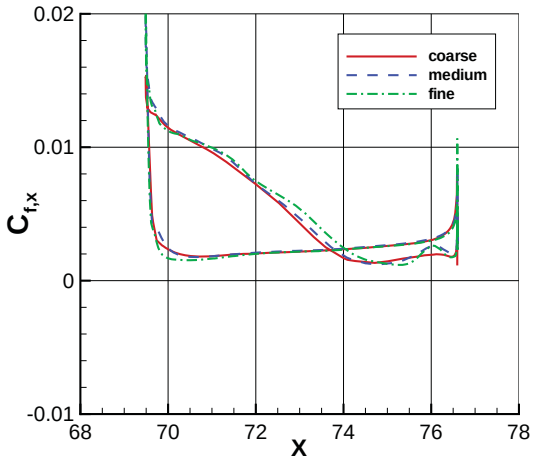

(f) Entry 021.01 (UH6 grid, SA)

Figure 11. Sampling of x-component of surface skin friction coefficients at 85% flap station, configuration 1, $\alpha = 13°$.

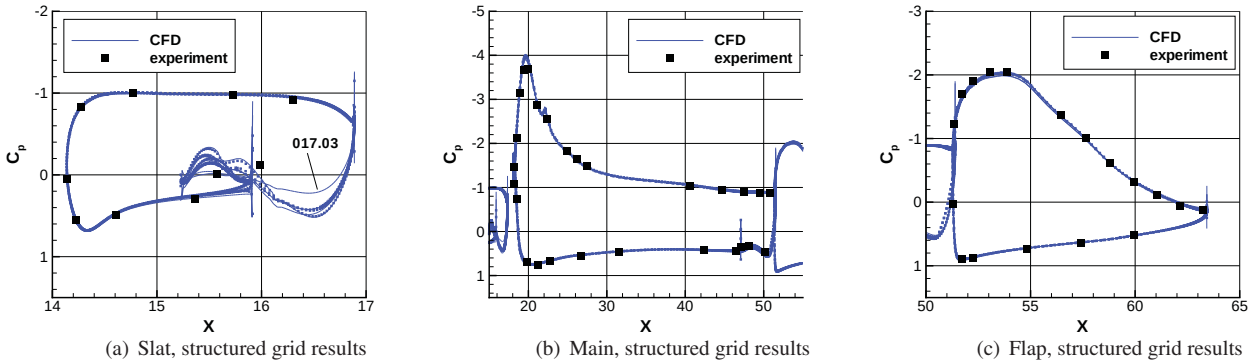

(a) Slat, structured grid results (b) Main, structured grid results (c) Flap, structured grid results

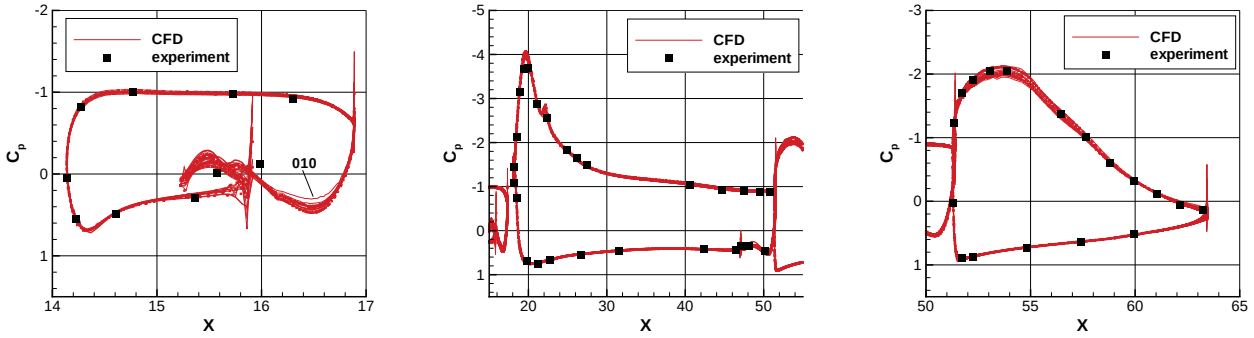

(d) Slat, unstructured grid results (e) Main, unstructured grid results (f) Flap, unstructured grid results

Figure 12. Surface pressure coefficients at 28% span station, configuration 1, $\alpha = 13^\circ$ (experiment at $\alpha = 12.991^\circ$), SA on fine grid only.

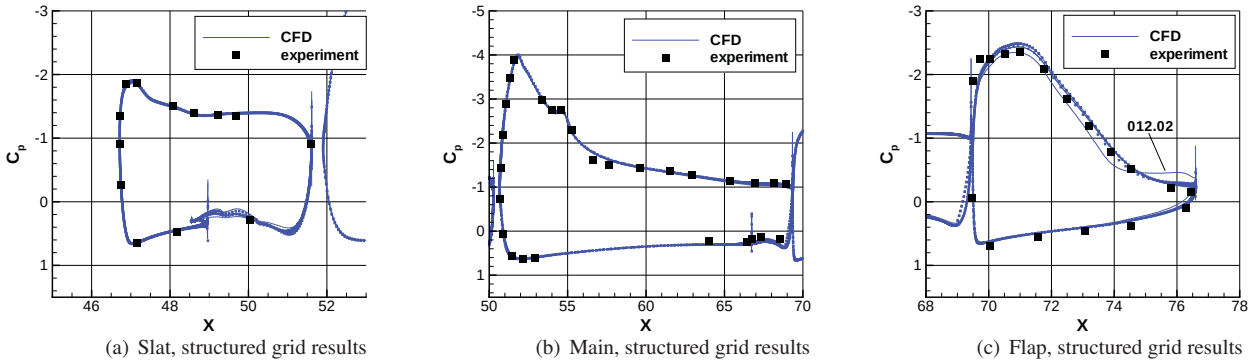

(a) Slat, structured grid results (b) Main, structured grid results (c) Flap, structured grid results

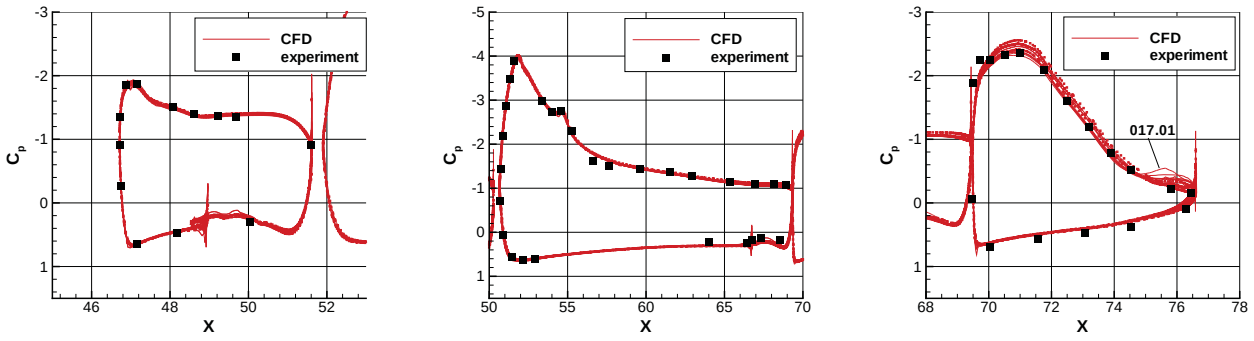

(d) Slat, unstructured grid results (e) Main, unstructured grid results (f) Flap, unstructured grid results

Figure 13. Surface pressure coefficients at 85% span station, configuration 1, $\alpha = 13^\circ$ (experiment at $\alpha = 12.991^\circ$), SA on fine grid only.

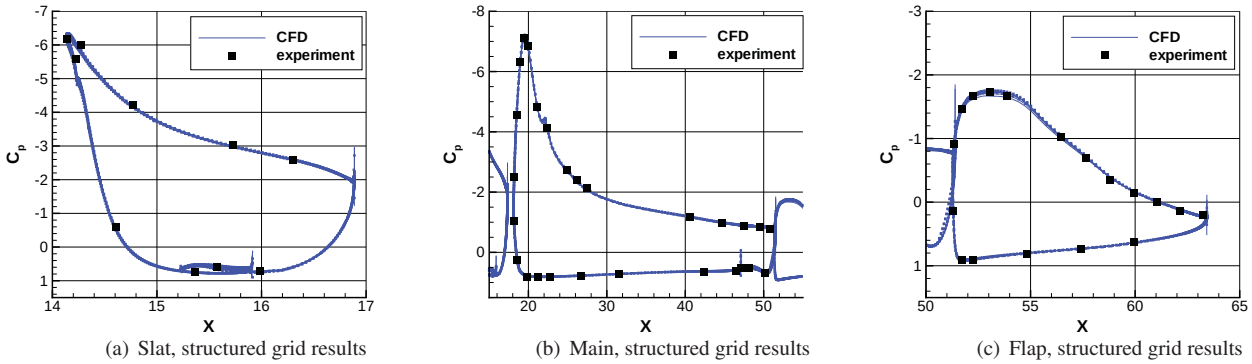

(a) Slat, structured grid results (b) Main, structured grid results (c) Flap, structured grid results

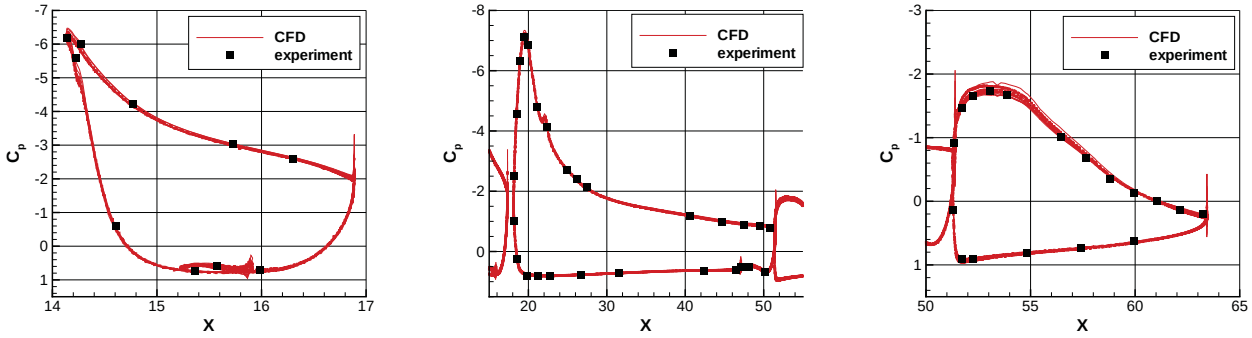

(d) Slat, unstructured grid results (e) Main, unstructured grid results (f) Flap, unstructured grid results

Figure 14. Surface pressure coefficients at 28% span station, configuration 1, $\alpha = 28°$ (experiment at $\alpha = 28.407°$), SA on fine grid only.

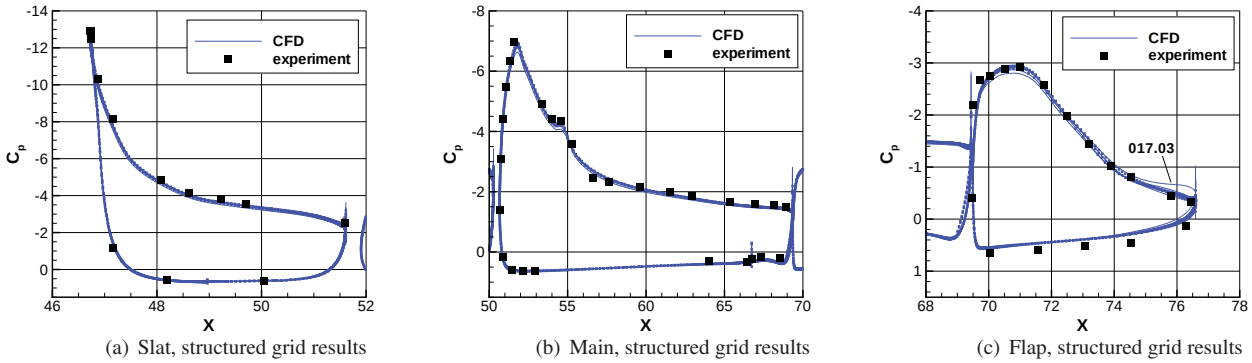

(a) Slat, structured grid results (b) Main, structured grid results (c) Flap, structured grid results

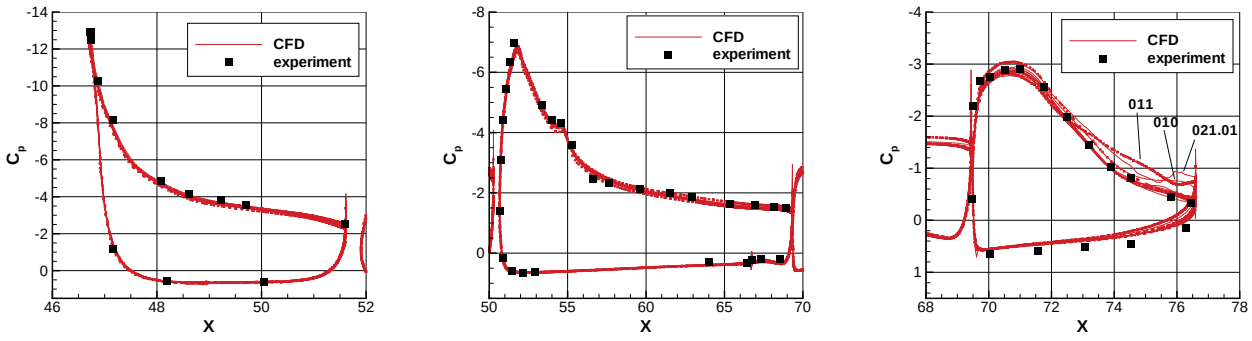

(d) Slat, unstructured grid results (e) Main, unstructured grid results (f) Flap, unstructured grid results

Figure 15. Surface pressure coefficients at 85% span station, configuration 1, $\alpha = 28°$ (experiment at $\alpha = 28.407°$), SA on fine grid only.

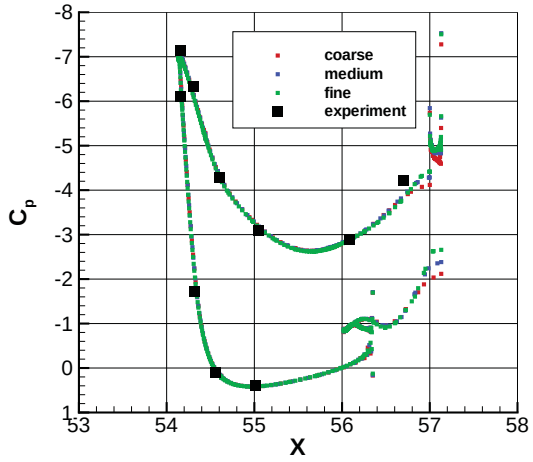

(a) Slat element, entry 018

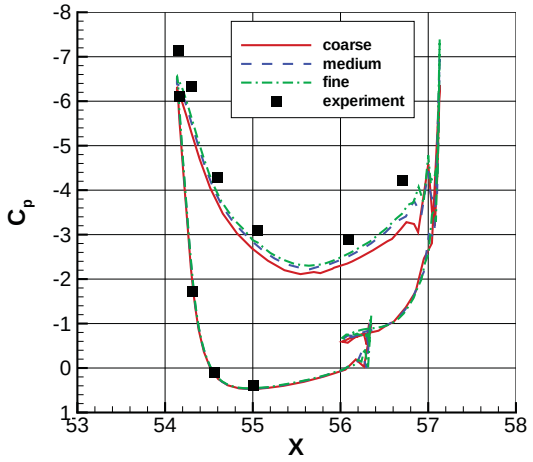

(b) Slat element, entry 010

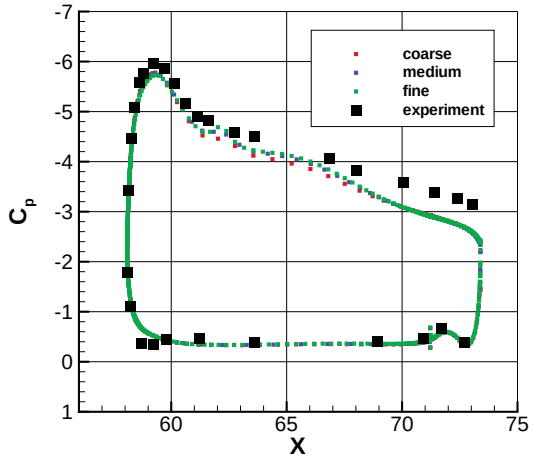

(c) Main element, entry 018

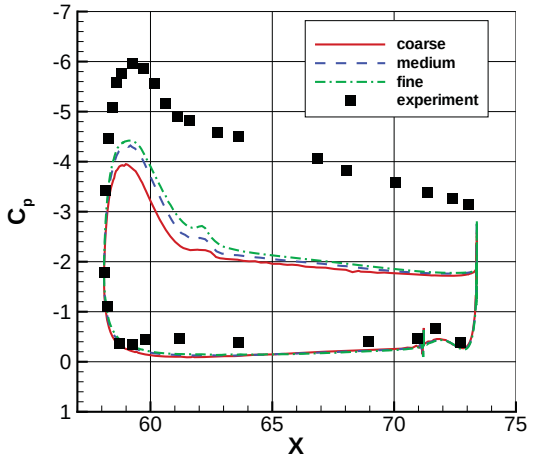

(d) Main element, entry 010

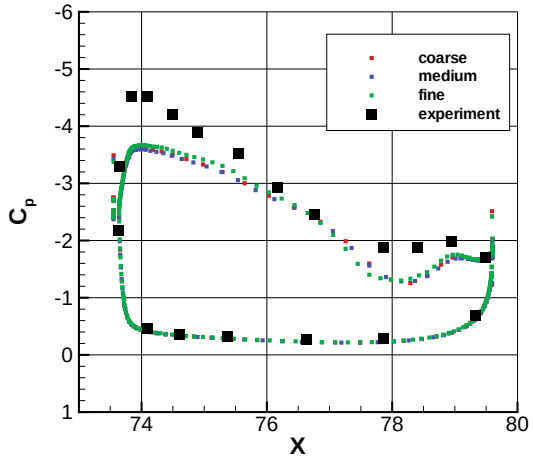

(e) Flap element, entry 018

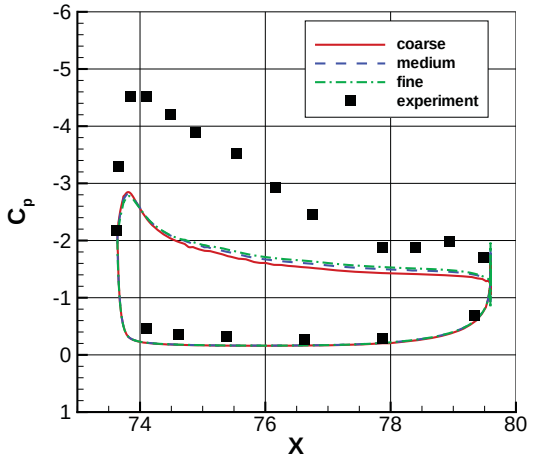

(f) Flap element, entry 010

Figure 16. Sampling of surface pressure coefficients at 98% span, configuration 1, $\alpha = 28°$ (experiment at $\alpha = 28.407°$).

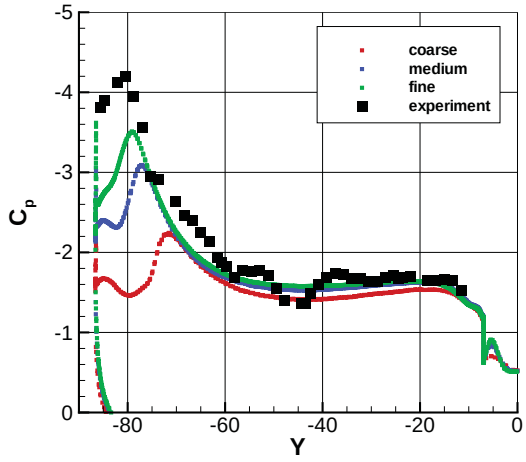

(a) Entry 013.02 (CFD++, UT5 grid, k-ε*, full)

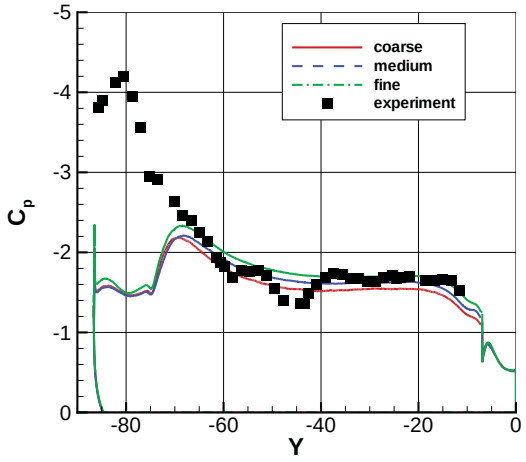

(b) Entry 002 (CFD++, UH13 grid, k-ε*, full)

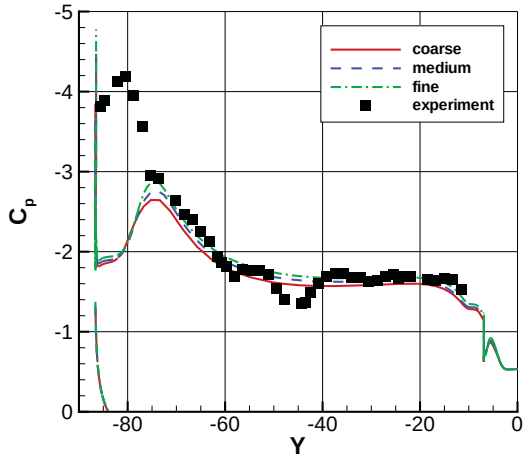

(c) Entry 017.03 (CFL3D, SX1 grid, SA, thin)

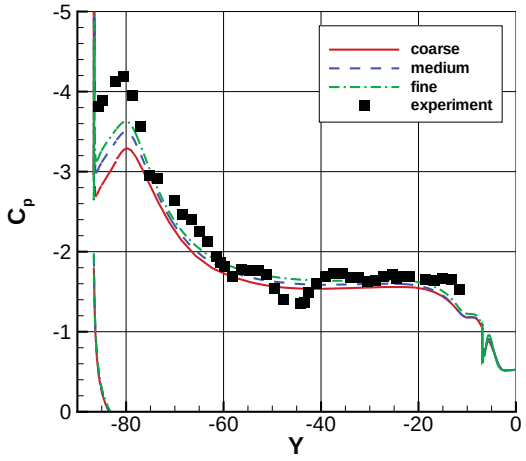

(d) Entry 017.05 (CFL3D, SX1 grid, SA, full)

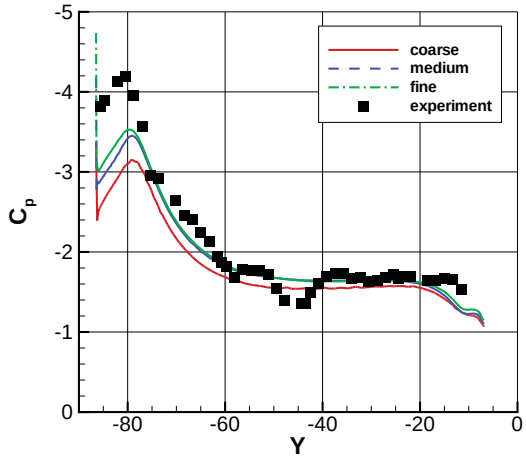

(e) Entry 015 (USM3D, UT4 grid, SA, full)

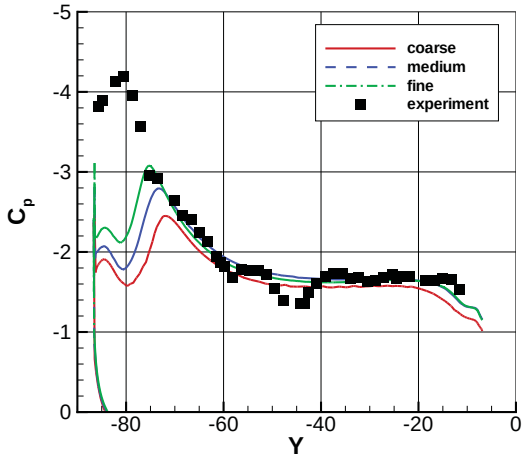

(f) Entry 020.02 (USM3D, UT4 grid, k-ω*, full)

Figure 17. Sampling of surface pressure coefficients at flap forward span station, configuration 1, $\alpha = 28°$ (experiment at $\alpha = 28.407°$).

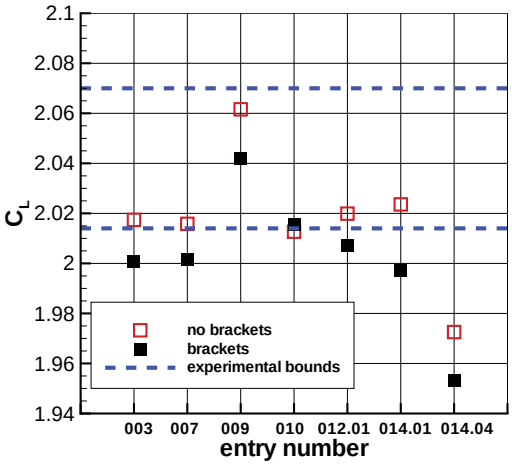

(a) C_L, $\alpha = 13°$

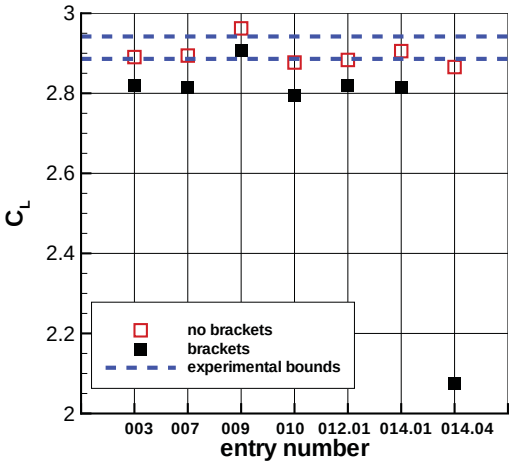

(b) C_L, $\alpha = 28°$

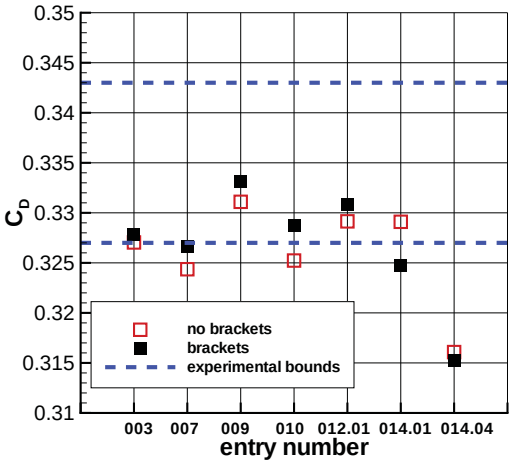

(c) C_D, $\alpha = 13°$

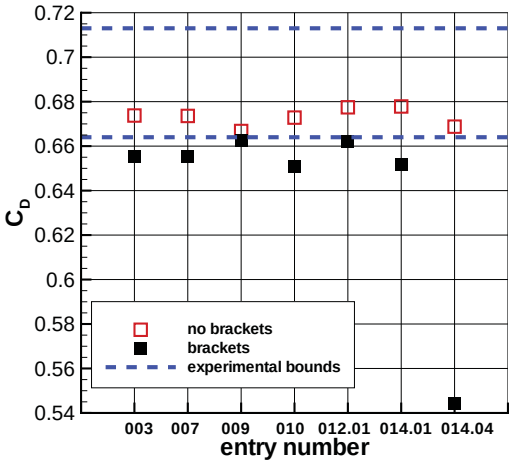

(d) C_D, $\alpha = 28°$

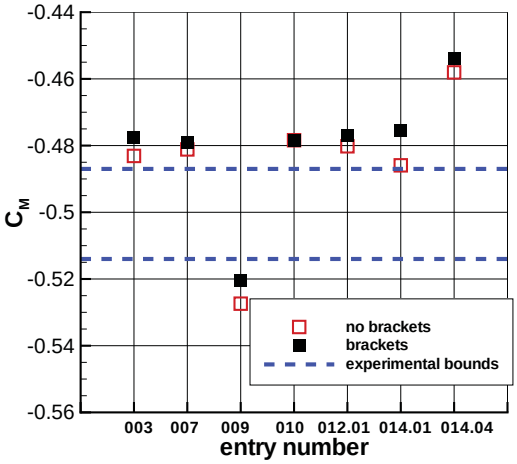

(e) C_M, $\alpha = 13°$

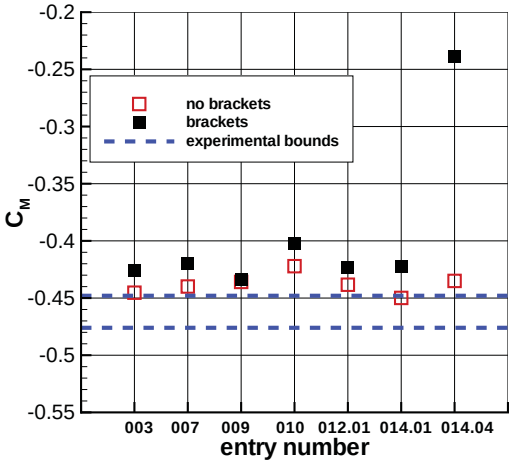

(f) C_M, $\alpha = 28°$

Figure 18. Effect of support brackets on forces and moments, configuration 1.

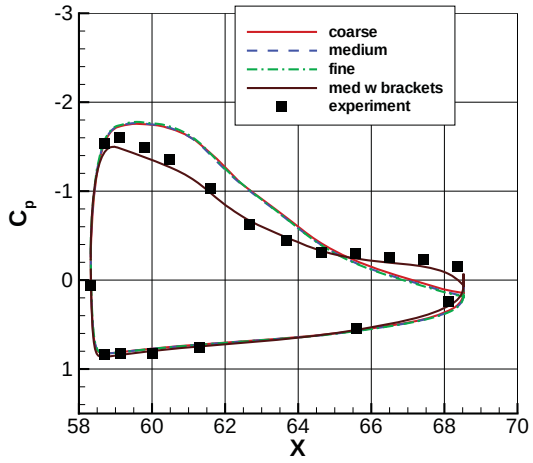

(a) Entry 003.01 at 50% flap span

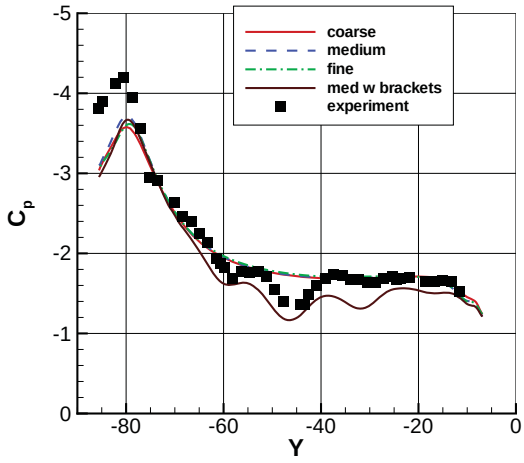

(b) Entry 003.01 at flap forward span station

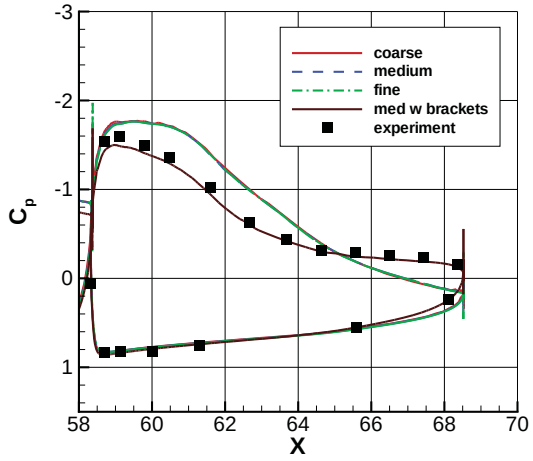

(c) Entry 007 at 50% flap span

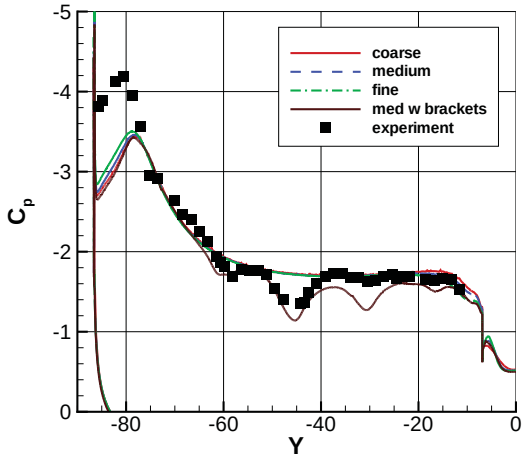

(d) Entry 007 at flap forward span station

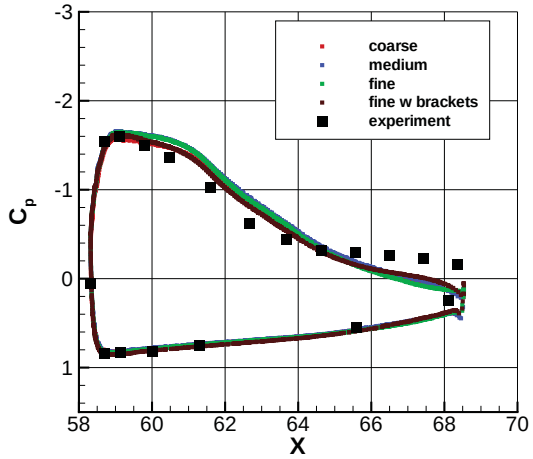

(e) Entry 009 at 50% flap span

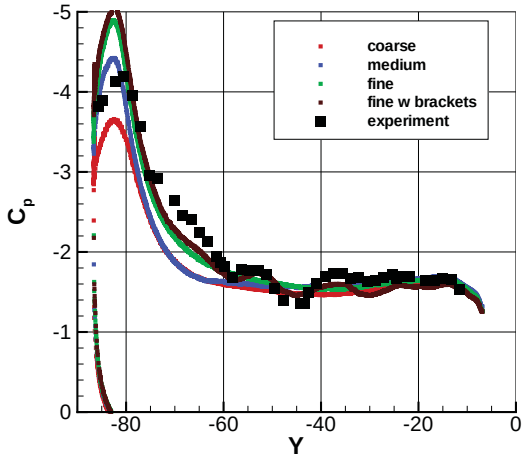

(f) Entry 009 at flap forward span station

Figure 19. Sample of effects of support brackets on pressure coefficients, configuration 1, $\alpha = 28°$ (experiment at $\alpha = 28.407°$).

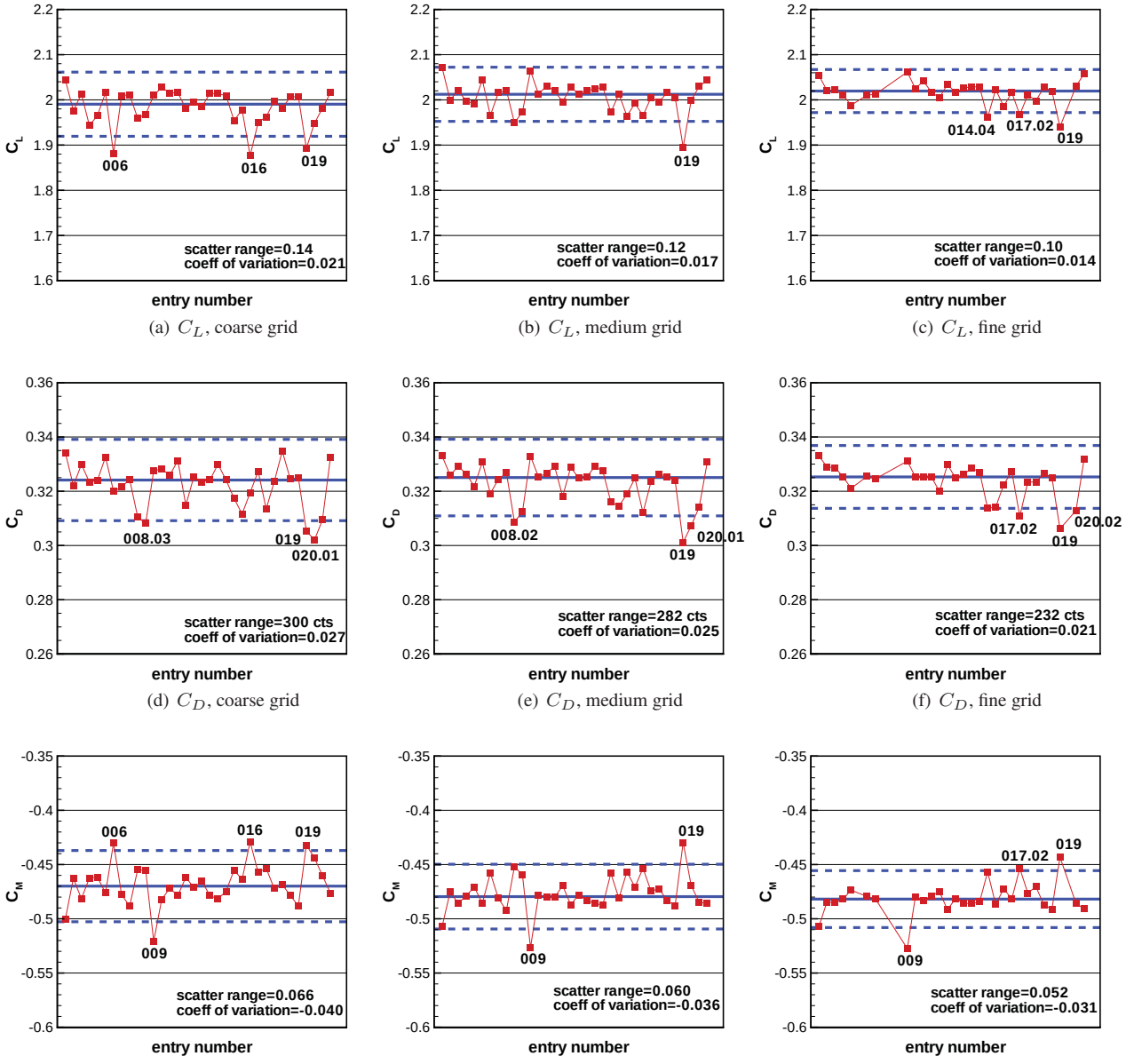

(a) C_L, coarse grid (b) C_L, medium grid (c) C_L, fine grid

(d) C_D, coarse grid (e) C_D, medium grid (f) C_D, fine grid

(g) C_M, coarse grid (h) C_M, medium grid (i) C_M, fine grid

Figure 20. Statistical analysis of all entries, configuration 1, $\alpha = 13°$; solid blue line is median of data, dashed blue lines are scatter limits.

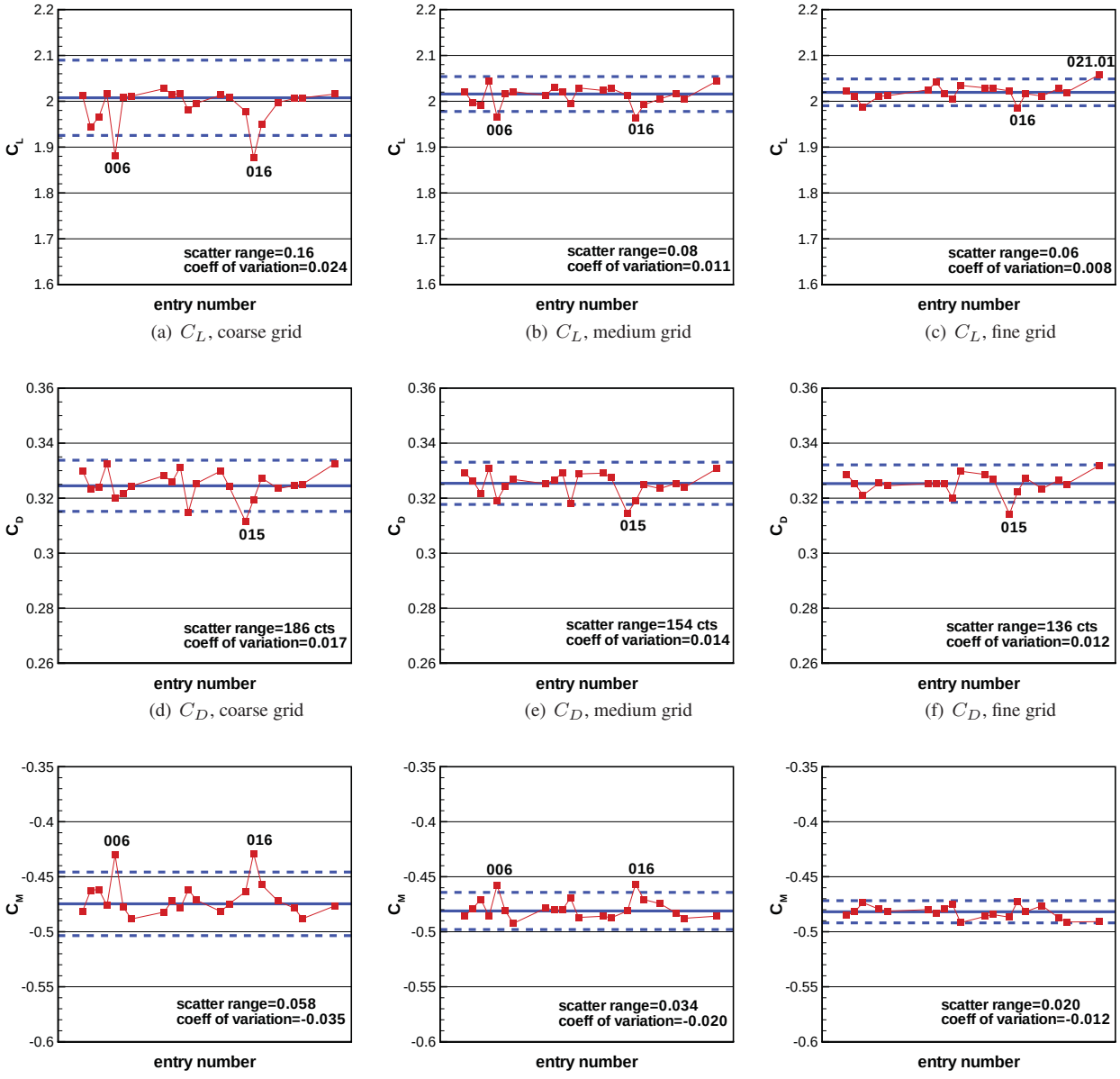

(a) C_L, coarse grid (b) C_L, medium grid (c) C_L, fine grid

(d) C_D, coarse grid (e) C_D, medium grid (f) C_D, fine grid

(g) C_M, coarse grid (h) C_M, medium grid (i) C_M, fine grid

Figure 21. Statistical analysis of SA entries, configuration 1, $\alpha = 13°$; solid blue line is median of data, dashed blue lines are scatter limits.

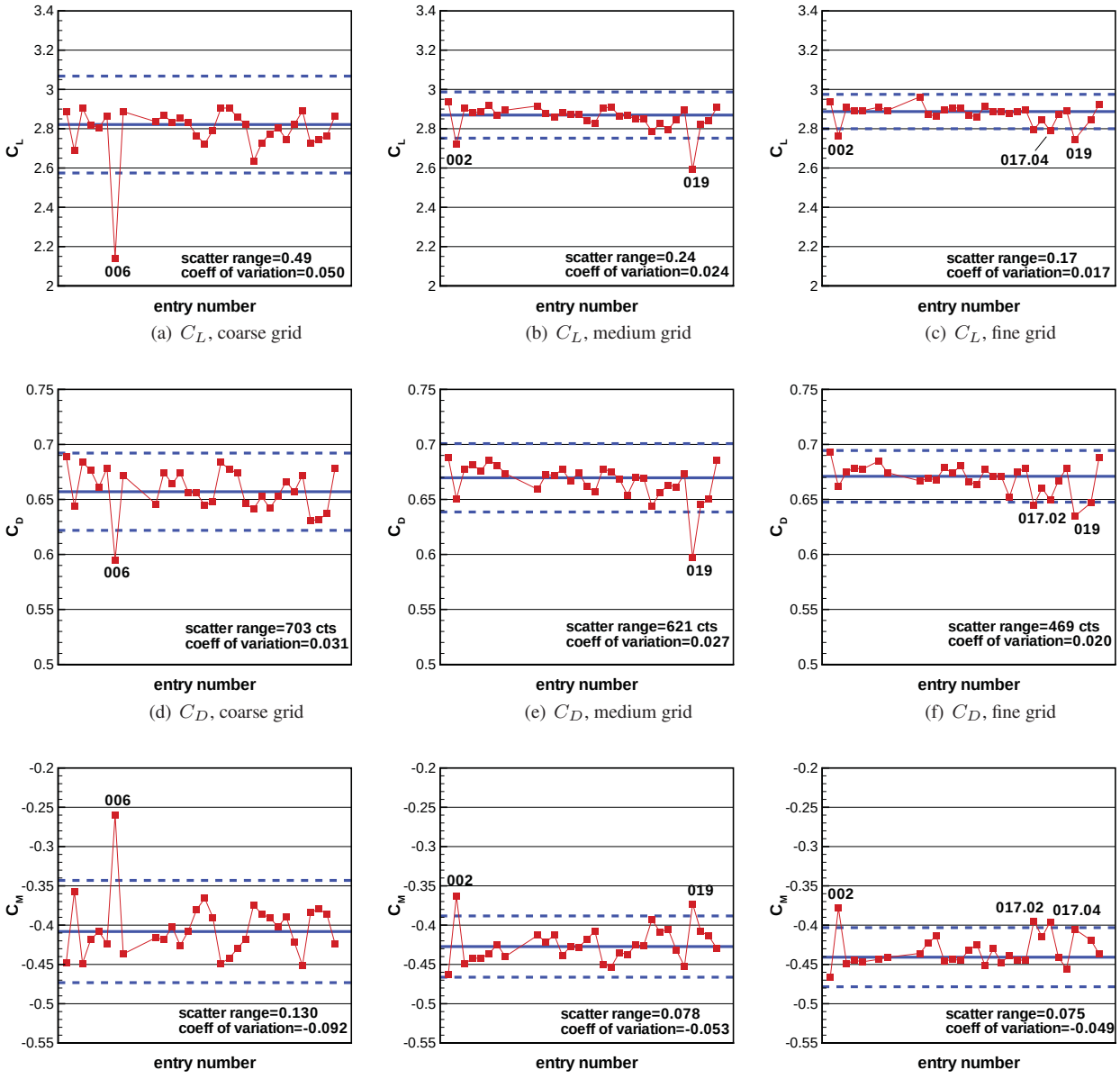

(a) C_L, coarse grid (b) C_L, medium grid (c) C_L, fine grid

(d) C_D, coarse grid (e) C_D, medium grid (f) C_D, fine grid

(g) C_M, coarse grid (h) C_M, medium grid (i) C_M, fine grid

Figure 22. Statistical analysis of all non-aberrant entries, configuration 1, $\alpha = 28°$; solid blue line is median of data, dashed blue lines are scatter limits.

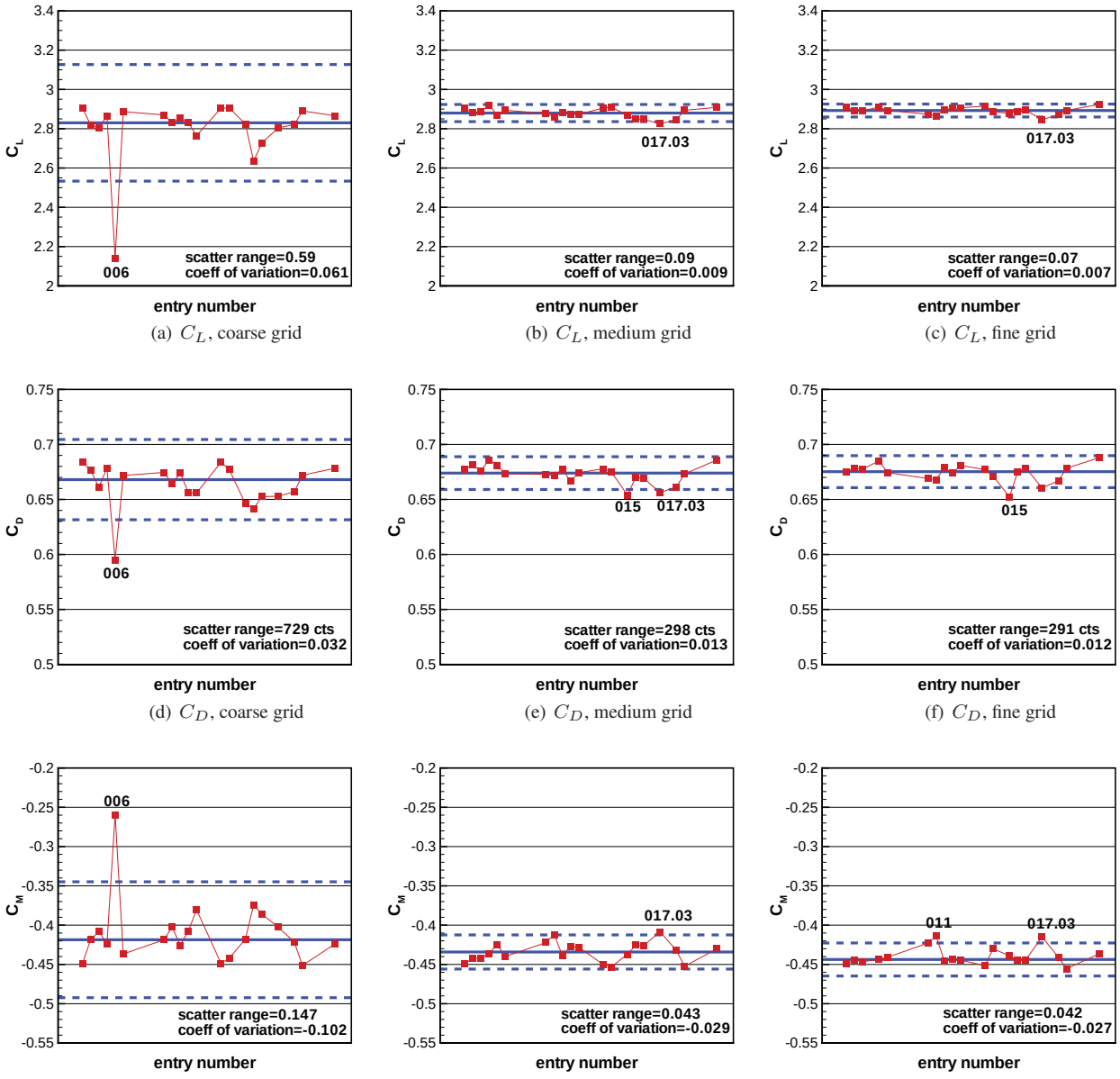

(a) C_L, coarse grid (b) C_L, medium grid (c) C_L, fine grid

(d) C_D, coarse grid (e) C_D, medium grid (f) C_D, fine grid

(g) C_M, coarse grid (h) C_M, medium grid (i) C_M, fine grid

Figure 23. Statistical analysis of non-aberrant SA entries, configuration 1, $\alpha = 28°$; solid blue line is median of data, dashed blue lines are scatter limits.

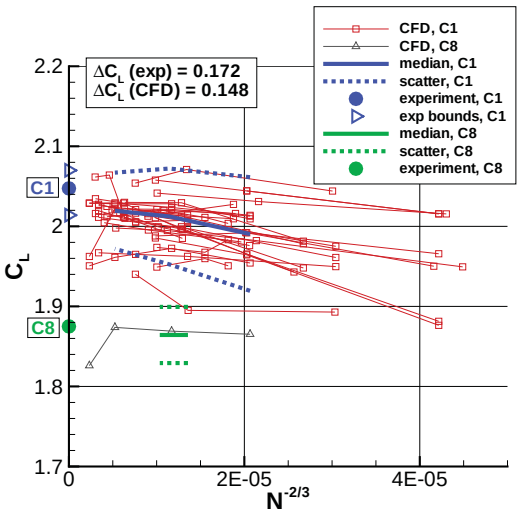

(a) C_L, all entries

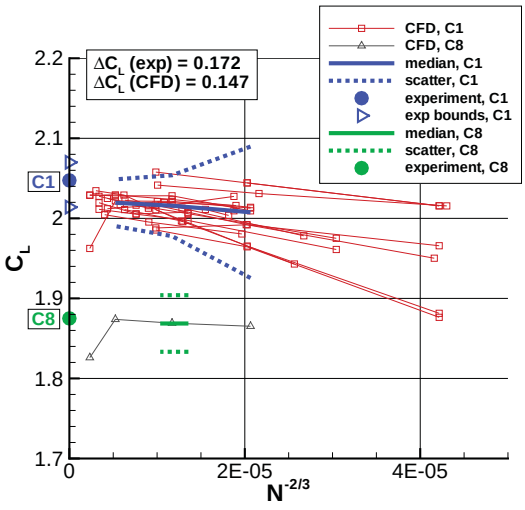

(b) C_L, SA entries

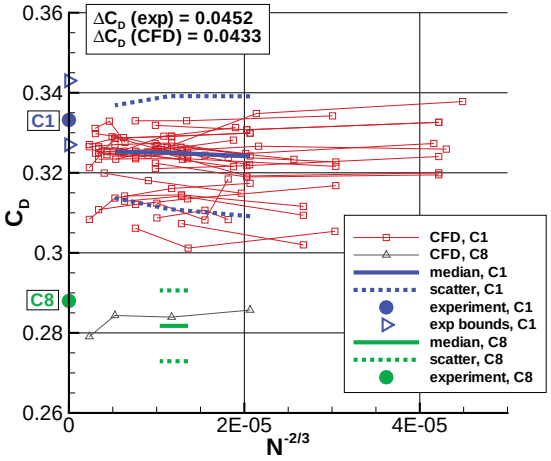

(c) C_D, all entries

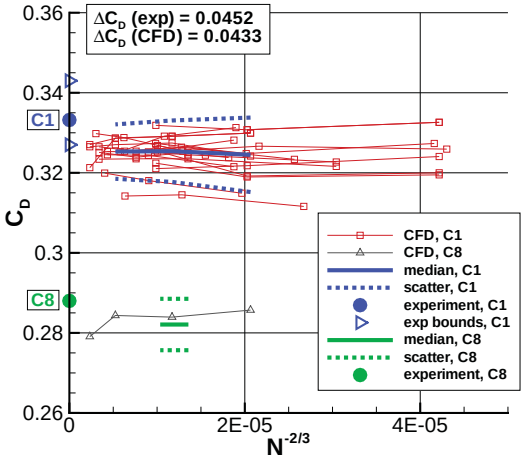

(d) C_D, SA entries

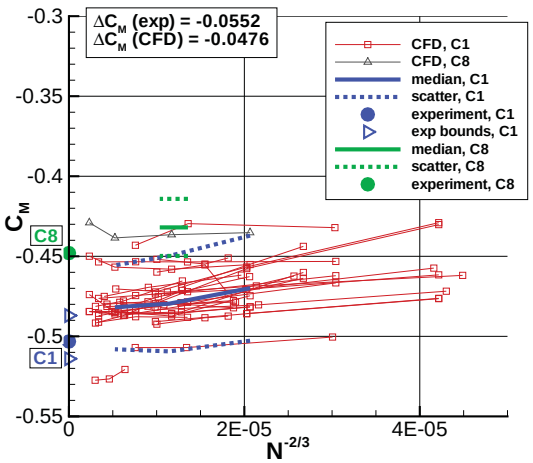

(e) C_M, all entries

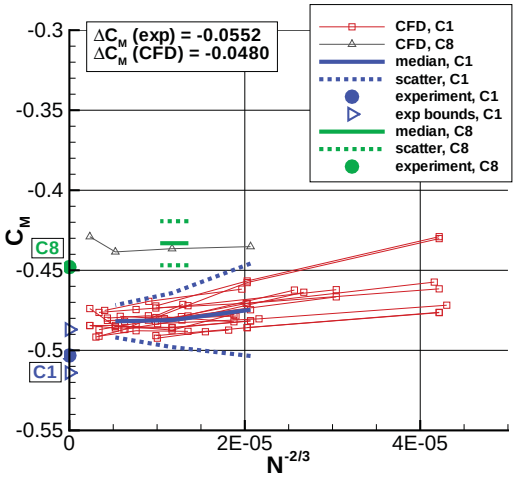

(f) C_M, SA entries

Figure 24. Grid convergence characteristics with scatter limits showing difference between configurations 1 and 8, $\alpha = 13°$.

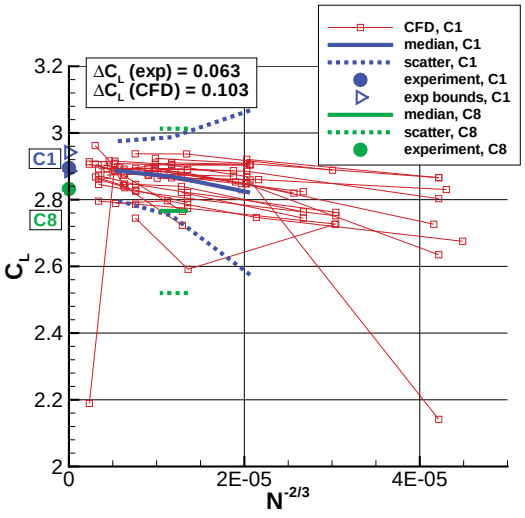

(a) C_L, all entries

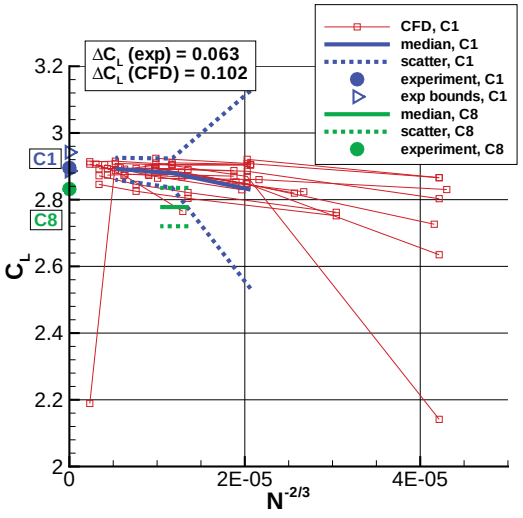

(b) C_L, SA entries

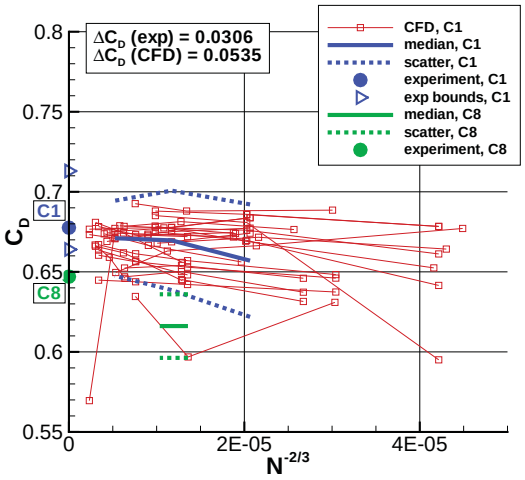

(c) C_D, all entries

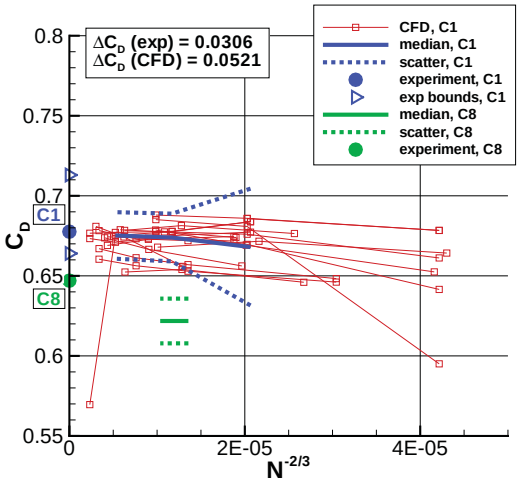

(d) C_D, SA entries

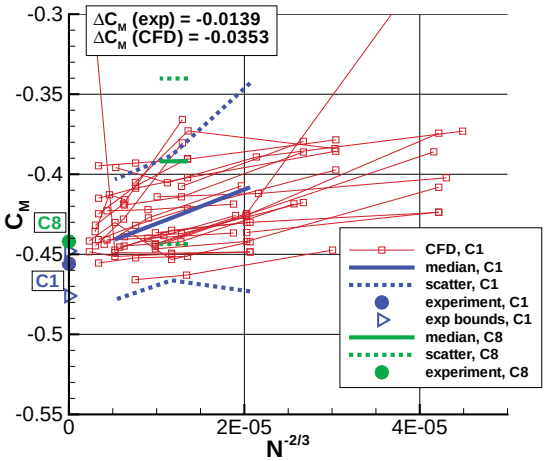

(e) C_M, all entries

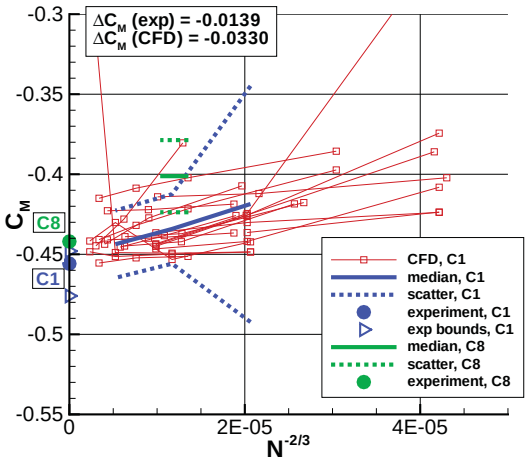

(f) C_M, SA entries

Figure 25. Grid convergence characteristics with scatter limits showing difference between configurations 1 and 8, $\alpha = 28°$.